REPORT DOCUMENTATION PAGE

AFRL-SR-BL-TR-98-

0454

ources,
of this
fferson

1. AGENCY USE ONLY (Leave blank)	2. REPORT DATE	3. REPORT TYPE AND DATES COVERED
	December 1997	Final Scientific Report.

4. TITLE AND SUBTITLE

Seismic Sources in China and Korea

5. FUNDING NUMBERS

grant F49620-94-1-0057

6. AUTHOR(S)

Paul G. Richards
Won-Young Kim

7. PERFORMING ORGANIZATION NAME(S) AND ADDRESS(ES)

Lamont-Doherty Earth Observatory of Columbia University
Palisades, NY 10964-8000

8. PERFORMING ORGANIZATION REPORT NUMBER

Phillips Laboratory
29 Randolph Road.
Hanscom AFB,
MA, 01731-3010

9. SPONSORING/MONITORING AGENCY NAME(S) AND ADDRESS(ES)

grant from Air Force Office of Scientific Research/NM

10. SPONSORING/MONITORING AGENCY REPORT NUMBER

11. SUPPLEMENTARY NOTES

12a. DISTRIBUTION/AVAILABILITY STATEMENT

Approved for public release; distribution unlimited

12b. DISTRIBUTION CODE

13. ABSTRACT (Maximum 200 words)

This final report is in four parts, consisting of: (1) a five-page summary of
Ph. D. thesis of Jinghua Shi entitled "Quantification of Earthquakes based on
Improved Estimates of Energy using Regional Waves"; (2) an application of methods
developed by this thesis, to estimate the spatial variability of seismic wave
attenuation in Western China; (3) a description of an unusual swarm of seismic
activity in Western China; and (4) a stand-alone paper entitled "Upper Mantle
Structure beneath Western China studied with the Cross-Array in Kazakhstan".

19980602 028

DTIC QUALITY INSPECTED 4

14. SUBJECT TERMS

test ban monitoring, seismic sources

15. NUMBER OF PAGES

16. PRICE CODE

17. SECURITY CLASSIFICATION OF REPORT	18. SECURITY CLASSIFICATION OF THIS PAGE	19. SECURITY CLASSIFICATION OF ABSTRACT	20. LIMITATION OF ABSTRACT
UNCLASSIFIED	UNCLASSIFIED	UNCLASSIFIED	UL

PL-TR

SEISMIC SOURCES IN CHINA AND KOREA

Paul G. Richards
Won-Young Kim

Lamont-Doherty Earth Observatory
  of Columbia University
Palisades, NY 10964

February 1998

Final Report

Part 1. A summary of the Ph. D. thesis of Jinghua Shi entitled

QUANTIFICATION OF EARTHQUAKES BASED ON IMPROVED ESTIMATES OF ENERGY USING REGIONAL WAVES

INVESTIGATIONS UNDERTAKEN

We report our studies of source and wave propagation parameters for regional earthquakes, especially the precision in measurement of earthquake strength, using seismic energy as the underlying property. The study is accomplished by analyzing the strongest regional seismic waves at distances in the range 20 - 1000 km, using frequencies across a wide band. Because of the demonstrable stability of root-mean-square (RMS) Lg amplitude and the relationship between RMS Lg and seismic energy, the study improves the accuracy of the traditional steps of correcting measured regional wave amplitudes for propagation effects, such as geometrical spreading and attenuation ($1/Q$) as a function of frequency, and on the scaling of regional earthquakes in northeastern United States, such as static stress drop and seismic energy.

RESULTS

We have carried out three projects:
- The method of spectral fitting a ω-square source model to the Lg displacement spectrum is applied to make a more reliable source corner frequency and stress drop estimates.
- $RMS\ Lg$ is defined from vertical component Lg waves, the quantity which has its underlying physical significance in terms of seismic energy and shows excellent consistency and stability for single station measurement.
- Based on the close relation between $RMS\ Lg$ and the radiated seismic energy, the empirical scaling of the total seismic energy (calculated from the source parameters with an assumed rupture model) with the network averaged $RMS\ Lg$ estimates is obtained both observationally and theoretically.

The Corner Frequencies and Stress Drops of Intraplate Earthquakes in the Northeastern United States

This study presents the estimation of stress drops for small to middle size intraplate earthquakes in the northeastern United States. The vertical component Sg and Lg waves of 49 earthquakes were analyzed. From our study, the source corner frequencies estimated by fitting the Lg displacement spectrum with the assumed ω-square source model are more consistent with the corner frequencies measured from empirical Green's function deconvolution method than those esti-

mated from the cross of horizontal low-frequency spectral asymptote and a line indicating the ω^{-2} decay after corner frequency (about 35% systematically smaller than the corner frequencies measured from empirical Green's function method). The source corner frequencies we estimated turned to be most appropriate for the small to middle size earthquakes.

The estimates of the stress drop for most of the events fall between 0.1 and 200 bars (Figure 1). The stress drops for events with the seismic moment less than about 2×10^{20} dyne-cm increase with increasing moment, then become less dependent on moment for the larger events. The critical value of 2×10^{20} dyne-cm seismic moment corresponds to nearly about magnitude 3. A dependence of stress drop on moment for smaller events suggests a breakdown in self-similarity below a threshold moment.

The Stability of RMS Lg Values in Estimating the Size of Regional Earthquakes in New York State and Adjacent Areas

Here, we investigate the property of *Lg* waves in terms of *RMS Lg* (root mean square value of *Lg* wave ground velocity amplitude within a certain group velocity range and scaled to 100 kilometer reference epicentral distance), especially the stability of *RMS Lg* values for natural earthquakes, in order to develop a magnitude scale that improves upon current procedures based on coda, or body waves, or maximum amplitudes.

From 52 regional earthquakes in the Northeastern United States, the *RMS Lg* values we obtained for epicentral distances (Δ) up to 900 kilometers decrease with Δ as about $\Delta^{-1.18}$ after correcting for anelastic frequency dependent attenuation. The measured *RMS Lg* values from different stations are quite consistent to each other, indicating excellent stability, as shown in Figure 2. *RMS Lg* values from single station measurement are consistent between different stations and are quite stable for regional earthquakes. The network averaged $Log_{10}(RMS\ Lg)$ against seismic moment, $Log_{10}(M_0)$, result in,

$$Log_{10}(RMS\ Lg)\ [nm/s]\ =\ 0.82 Log_{10}(M_0)\ [dyne-cm]\ -12.70$$

with orthogonal standard deviation of 0.12 $Log_{10}(M_0)$ unit.

Determination of Seismic Energy from Lg Waves

Lg waves, which can be treated as wide angle reflection of shear waves trapped within the crust, are the dominant feature of seismograms for regional earthquakes, and become very useful for regional earthquake analysis, specifically for the estimation of radiated seismic energy. In this study, we make the estimates of seismic energy from regional *Lg* waves, using broadband frequency data of regional earthquakes in a region where the attenuation information is well determined. We have demonstrated the seismic energy radiation for different classes of earthquakes using *Lg* waves in terms of *RMS Lg*, and obtained the scaling of the total seismic energy of earthquakes (using an assumed source model) with seismic energy measured from *Lg* waves (*RMS Lg*) both synthetically and observationally for regional earthquakes in the northeastern United States.

The relation between the total seismic energy calculated from the earthquake source (assuming *Boatwright's* (1980) Deceleration model) and the network averaged *RMS Lg* value can be expressed as (Figure 3),
For 52 regional earthquakes:

$$log_{10}(E_s) \; [ergs] \; = 2.07 log_{10}(RMS \; Lg) \; [nm/s] + 8.91 \qquad \sigma = 0.15$$

From the synthetics:
    for vertical strike-slip,

$$log_{10}(E_s) \; [ergs] \; = 2 log_{10}(RMS \; Lg) \; [nm/s] + 9.014 \qquad STD = 0.03 \; ;$$

for 30° thrust fault,

$$log_{10}(E_s) \; [ergs] \; = 2 log_{10}(RMS \; Lg) \; [nm/s] + 8.718 \qquad STD = 0.03 \; ;$$

for 60° normal fault,

$$log_{10}(E_s) \; [ergs] \; = 2 log_{10}(RMS \; Lg) \; [nm/s] + 8.715 \qquad STD = 0.03 \; .$$

The seismic data upon which our results are based are available in AH format. The contact person is Jinghua Shi (phone: 914-365-8460; Email: jinghua@ldeo.columbia.edu).

NON-TECHNICAL SUMMARY

In this project, we studied the use of Lg waves in terms of the precise scaling of regional earthquake strength, such as the stress drop and seismic energy release. We defined a quantity, RMS Lg (root-mean-square of Lg amplitude scaled to 100 kilometer reference distance) wide frequency integration of vertical component Lg signals within certain group velocity window. We proved that, RMS Lg has a physical significance in terms of seismic energy, shows excellent consistency and stability even for single station measurement. Based on the close relation between RMS Lg and the radiated seismic energy, the absolute scaling is obtained between the total seismic energy from earthquake source and the network averaged RMS Lg estimates.

REPORTS PUBLISHED OR SUBMITTED FOR PUBLICATION

Shi, Jinghua, Won-Young Kim and Paul G. Richards, Variability of crustal attenuation in the northeastern United States from *Lg* waves, *Journal of Geophysical Research*, **101**, 25231–25242, 1996 (correction, **102**, 11899, 1997).

Shi, Jinghua, Won-Young Kim and Paul G. Richards, The stability of RMS *Lg* values in estimating the size of regional earthquakes in New York State and adjacent areas, submitted to *Seismological Review Letters*, January 1998.

Shi, Jinghua, Won-Young Kim, and Paul G. Richards, The corner frequencies and stress drops of intraplate earthquakes in the Northeastern United States, *Bulletin of the Seismological Society of America*, in press for issue of April 1998.

Shi, Jinghua, Paul G. Richards, and Won-Young Kim, Determination of seismic energy from *Lg* waves, submitted to *Bulletin of the Seismological Society of America*, January 1998.

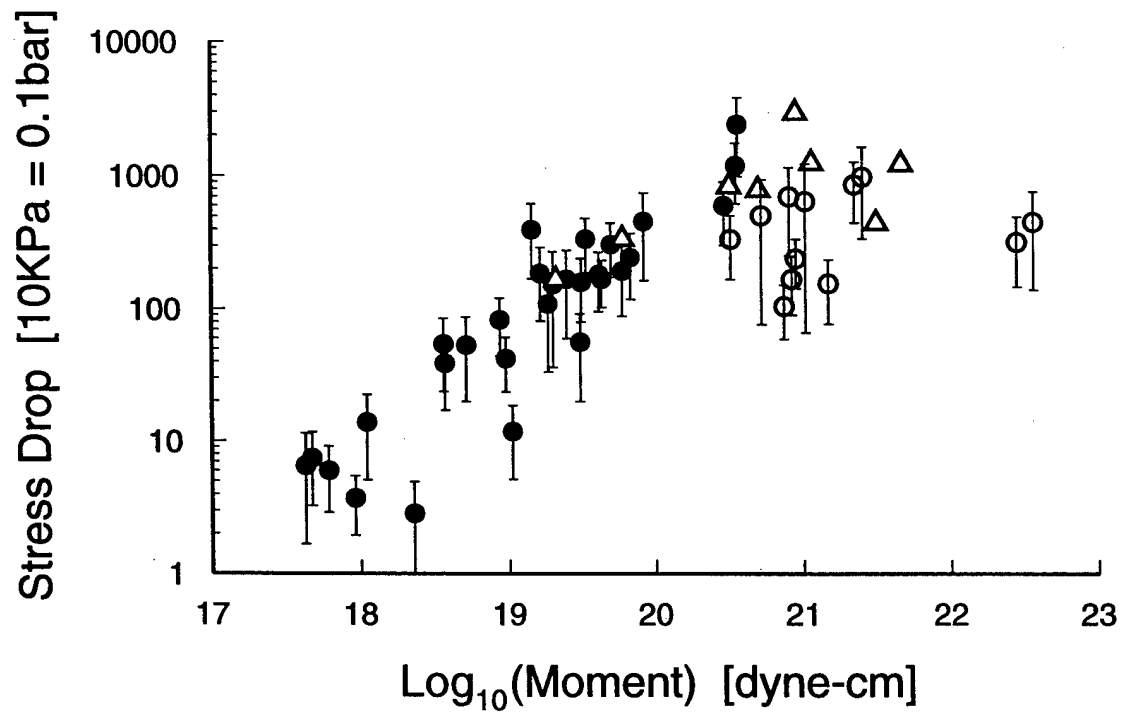Figure 1. The relation between the static stress drop and the seismic moment with the error bar (the mean of error in the event network average). The filled circles are for the events for which only short-period data are available. The empty circles are for the events that have broadband data. The triangles are for the events whose source corner frequencies were estimated from empirical Green's function method.
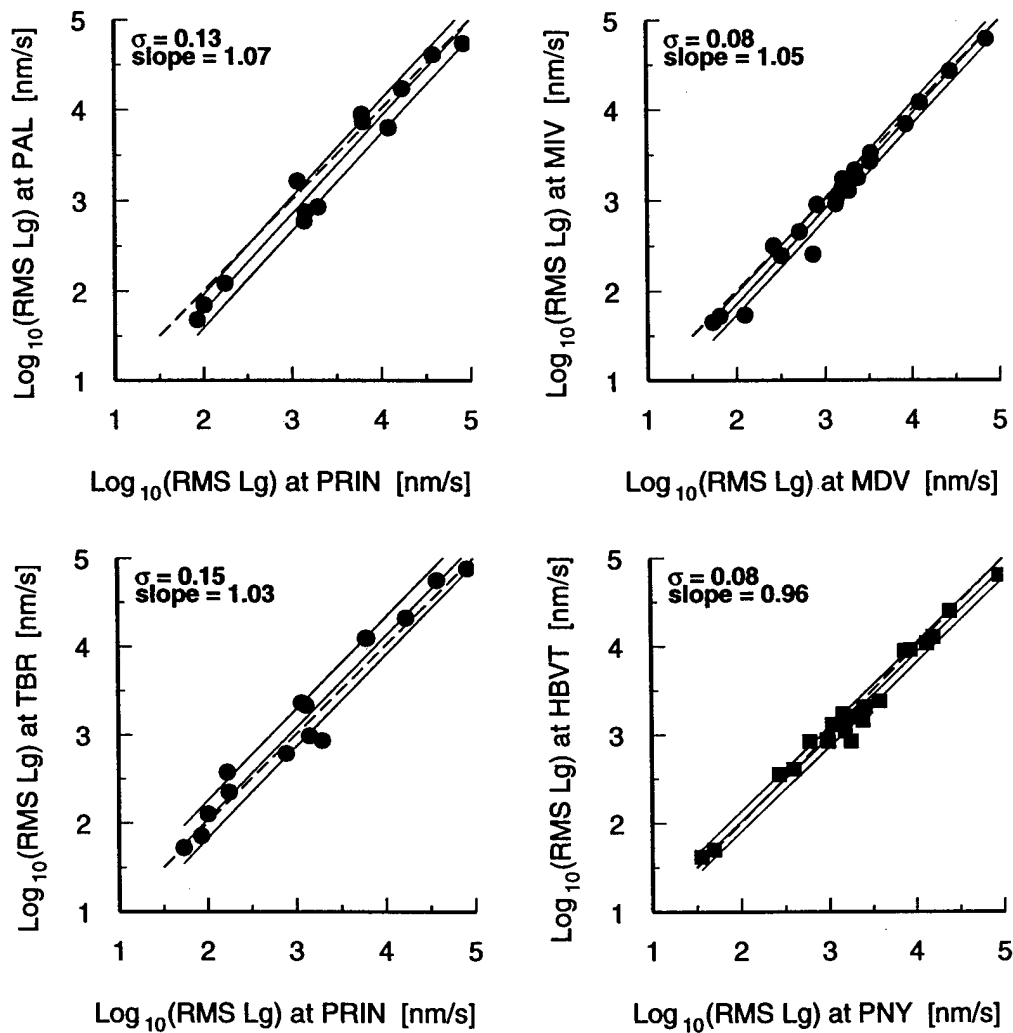
Figure 2. Orthogonal regressions of log(*RMS Lg*) at two stations are plotted, showing the stability of single station's *RMS Lg* measurements. Three solid lines indicate the range of one standard deviation (σ). Dashed lines show the ideal consistency relation between *RMS Lg* values from two stations.

$$Log_{10}(Es)[erg] = 2.07Log_{10}(RMS\ Lg)[nm/s] + 8.91$$

$$\sigma = 0.15$$

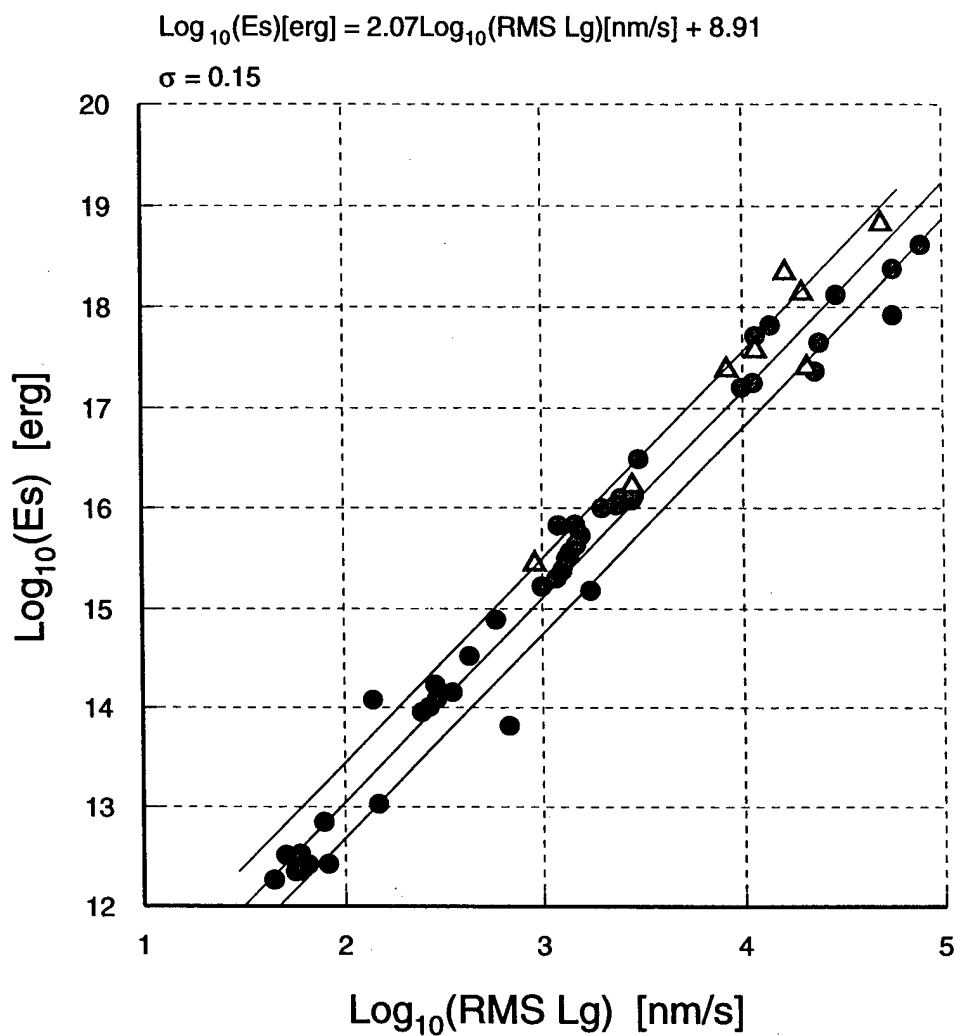Figure 3. The regression of seismic energies calculated from the source parameters with the network averaged *RMS Lg* values for 52 regional earthquakes in northeastern United States is plotted. We assumed the source as Boatwright's Deceleration model in seismic energy calculation. The network averaged *RMS Lg* values are measured from vertical component *Sg* and Lg signals within a group velocity window from 3.6 - 3.0 km/s.

Part 2. An application of methods developed by the thesis, described in Part 1, to estimate the spatial variability of seismic wave attenuation in Western China.

Attenuation Variation in Xinjiang, China

Jinghua Shi, Paul G. Richards, and Liping Gao

Lamont-Doherty Earth Observatory of Columbia University

Palisades, NY 10964

ABSTRACT

We have applied the empirical Green's function method to event pairs recorded by the single station WMQ (Urumqi, China) from 1988 - 1989 to determine the source corner frequencies of the 28 larger events in these pairs, and have estimated the crustal averaged attenuation quality factor Q around station WMQ. 28 path-averaged quality factor Q values were obtained from epicentral distances ranging between 90 to 260 kilometers. We found that: the Q values for the paths crossing the Tien Shan mountains are the lowest, about 500 - 600; the Q values for the paths along the Tien Shan mountains are relatively higher, about 700; and the Q values for the paths through the basin to the southeast of WMQ are the highest in the three groups, about 800 - 900. The spatial inhomogeneity in attenuation quality factor Q near station WMQ shows good correlation with the tectonic structure in the region.

INTRODUCTION

The Tien Shan Range extends east-west for at least 2500 km. This large tectonic belt in Central Asia lies just behind the collision of India into the Asia plate and forms the most active intracontinental mountain range in the world. This region is very complex both from geology and topography, and there are many active thrust and strike-slip faults (*Tapponnier and Molnar*, 1979). As a result, the seismic properties in the region will have large spatial variation.

From the perspective of western scientists, the region is remote and has not been thoroughly studied. But it has become interesting to seismologists because of tectonic and political reasons. The development of methodology makes it possible to study the Tien Shan Range seismologically even from single station.

The seismographic station WMQ is located within this complex region, at the north boundary of Tien Shan. The available data from WMQ in the late 1980's to the mid 1990's consist of three component continuously recorded broadband and triggered short period digital records, which are well suited for recording regional seismic waves. We selected the period 1988-1989 because we have good bulletin information in these years, from Chinese seismologists, and hence have epicenter parameters for the sources of our digital signals.

Patton et al. (1985) studied the regional structure in the path from East Kazakhstan to the Dzhungaria basin which is north west of WMQ and Tien Shan. The structure in Tien Shan and the Tarim basin, to the south of Tien Shan are likely to show significant differences because of the effects of the collision between Indian and Asian plates. *Gao and Richards* (1995) presented evidence that the depth of Moho in Xinjiang is quite deep (46

kilometers), and that there is a lateral velocity inhomogeneity near the WMQ station based on the analysis of a polarization anomaly from P waves from teleseismic sources.

In this paper, we shall focus on the spatial attenuation variation of shear waves in the region near WMQ. Our overall goal is to achieve a better understanding of attenuation, in a detailed study of the propagation of seismic waves to assist in the interpretation of seismic energy release in this region.

ATTENUATION ESTIMATION

Seismic attenuation represents the loss of seismic energy as a wave propagates, over and above what is expected from geometrical spreading. Attenuation is usually frequency dependent especially for bands that include high frequency signals.

From discussions by *Atkinson* (1992) and *Shi et al.* (1996), the geometrical spreading of Lg waves at short distances is itself complex and does not follow theory such as the $[\Delta^{1/3}\sin\Delta^{1/2}]^{-1}$ dependence predicted for Airy phases. The direct inversion of attenuation quality factors from regional earthquakes is therefore difficult and probably requires the use of laterally varying structures.

However, the empirical Green's function method makes it possible for us to first obtain the source information and then to estimate the path-dependent attenuation factor Q from fitting the Lg displacement spectrum over a wide frequency range by using the known source information. This process does not require the geometrical spreading factor which is so uncertain for regional earthquakes.

We assume the frequency dependent attenuation spectrum along the path from event i to station j as,

$$B_{ij}(f) = \exp\left\{\frac{-\pi f \Delta_{ij}}{v Q_{ij}}\right\} = \exp\left\{\frac{-\pi f t_{ij}}{Q_{ij}}\right\},$$

with Δ being the epicentral distance, v the S-wave velocity, and t the travel time. The attenuation quality factor Q is usually considered to be frequency dependent (*e.g. Singh and Herrmann*, 1983; *Campillo*, 1987) and we assumed Q as,

$$Q = Q_0 f^{\eta},$$

with Q_0 = the quality factor value at 1 Hz, and η = the exponent parameter of the quality factor which is constant over the frequency band of interest (*e.g. Mitchell*, 1980).

In order to obtain an accurate estimate of the two unknown parameters in the attenuation quality factor, we must first eliminate the trade-off problems of source corner frequency and Q_0, which can give the same shape of the signal spectrum by increasing one parameter and decreasing the other. However, one of these parameters is determined by the source of the event, and the other parameter is determined by the propagation path from event to stations. Based on this difference, we first use the empirical Green's function deconvolution process to obtain the source information, especially the corner frequency of the event. Then we introduce the corner frequency estimated from empirical Green's function deconvolution into the process of attenuation analysis. As shown by *Shi et al.* (1996), this two step analysis makes it possible to measure the two spectral parameters accurately, and give good information for the path dependent spatial variation of the attenuation quality factor.

In the empirical Green's function deconvolution process, we require an event pair with magnitude different enough but having the same wave propagation path and same source mechanism, so that the smaller event can be treated as the empirical Green's function of the larger event and the deconvolution of the same phases of the two events will only contain source information. From the deconvolution, which is a spectral ratio in the frequency domain, we can estimate the corner frequency of the larger event in the pair using an optimizing method. In order to simplify the problem, we assume the source has only one corner frequency, which gives an upper limit for the size of the larger event in each pair. Also the signal to noise ratio of the smaller event needs to be good enough in the frequency band for analysis, and this gives a limit on the epicentral distance of the events and a lower limit on the size of the smaller event in the pair.

The observed spectrum $A_{ij}(f)$ of event i at station j can be modelled as,

$$A_{ij}(f) = S_i(f) \cdot I_j(f) \cdot F_j(f) \cdot R_{ij}^{-1} \cdot B_{ij}(f),$$

with source spectrum

$$S_i(f) = \Omega_{0i} \cdot R_{\theta\phi} \cdot \frac{f_{ci}^{-3}}{1 + (f/f_{ci})^2}.$$

Here Ω_{0i} is the low frequency spectral asymptote and is proportional to the scalar seismic moment. $R_{\theta\phi}$ is the radiation pattern parameter, and f_c is the source corner frequency based on Aki's (1967) ω^2 model. Parameter $I(f)$ represents the instrument response, $F(f)$ the site response, R the geometrical spreading, and B_{ij} the event to station path-averaged attenuation term in frequency domain.

The factors, $I(f)$, $F(f)$, R and B_{ij} cancel out in the spectral ratio we are considering, so that

$$r(f) = C_0 \cdot \frac{1 + (f/f_{c2})^2}{1 + (f/f_{c1})^2} \cdot \left(\frac{f_{c1}}{f_{c2}}\right)^{-3}.$$

C_0 is the ratio of Ω_{01} and Ω_{02}.

We use an optimization method in which corner frequencies f_{c1} and f_{c2} are varied on a grid to minimize the root mean square of $r_{OBS}(f) - r(f)$ and to find the best fit f_{c1}, where $r_{OBS}(f)$ is the spectral ratio from an observed data pair.

The second step is to estimate the two parameters Q_0 and η from the S and Lg displacement spectrum of the signal. We define a prediction root mean square error,

$$E = \left\| \ln\left(A_{ij}(f) \cdot I_j^{-1}(f)\right) - \left[\ln\left(\frac{f_c^{-3}}{1 + (f/f_c)^2}\right) - \left(\frac{-\pi f \Delta_{ij}}{v Q_{0ij} f^{\eta_{ij}}}\right) \right] - C \right\|,$$

where $\| \; \|$ denotes the root mean square error and $C = log_e(\Omega_{0i} \cdot R_{ij}^{-1} \cdot F_j)$ which is considered as frequency independent. Performing a grid search over Q_0 and η, with the above C being the one that minimizes E, we choose the best fit of Q_0 and η for each path, given corner frequency, f_c, of the event. When we assume F_j as frequency independent, we are ignoring the site response which can be a significant factor (*e.g., Chun et al.*, 1987). As a result, the variation in the attenuation quality factor Q that we have estimated includes the site effect near the source and receiver region.

DATA PROCESSING

The seismograms used in this study were recorded by CDSN (Chinese Digital Seismographic Network) station, WMQ (Urumqi). There are two instrument responses, one flat to velocity from 0.05 to 4 Hz and recorded at 20 sample/s, another flat to velocity from 1 to 8 Hz and recorded at 40 sample/s.

We selected 41 event pairs from 1988 to 1989 based on the requirements of the empirical Green's function method. The station WMQ is the nearest digital station to the Lop Nor nuclear test site in Xinjiang, China. The events we selected (Table 1) are all natural earthquakes that happened quite near to the test site, with paths to WMQ crossing Tien Shan Mountains. The study of these events is very useful to analyzing the structure in this region. Each pair of events selected have similar foci location, similar source mechanism, and the waves from both events traveled a similar path and are recorded by the WMQ station with similar wave forms, but with different magnitude (Figure 1). Some pairs have the same larger events and there are only 28 independent larger events in the total set of pairs. The pair events generally have focal depth within 0 - 20 km range, magnitude from 2.7 - 5.1 m_b magnitude for larger events, and 2.5 - 3.5 m_b for smaller events (Table 1). The spatial distribution of these events are mainly south and southwest of the WMQ station, ranging from 90 - 260 km epicentral distance.

We computed the displacement amplitude spectrum of vertical component P waves using about 2.0 seconds window after the first P arrival (mainly Pg), and vertical component S and Lg waves within a group velocity window from 3.0 to 3.6 km/s. The signal to noise ratio for both events in each pair is well above 2. The instrument response was removed before calculating the displacement spectrum.

From simplicity in analysis, we assumed the source for both events in the pairs con forms to Aki's ω^2 model with one corner frequency for the source spectrum, and we ignored the directivity effect of the source on corner frequency measurement. Discrepancies among estimates for large local events may come from violations of the point source approximation and possible directivity of the source, and one station estimation of f_c can have large bias. However, for earthquakes with magnitude less than 5, the duration of the source is only about 1 - 2 seconds, therefore the source may not be so complex as having two corner frequencies in its spectrum, and the directivity is not so significant. From our previous work in Northeastern United States earthquakes (*Shi et al.* 1998), the uncertainty caused by these simplifications is not larger than 2 Hz in corner frequency estimation.

Figure 2 is an example of our procedure for estimating the corner frequency of the larger event in the pair by searching the optimal corner frequency f_{c1} and f_{c2} with ω^2 source model and frequency dependent Q simulation. Usually we only estimated corner frequency for the larger event in the pair and fixed the corner frequency of the smaller event f_{c2} at some value. The uncertainty in f_{c2} does not effect the estimation of f_{c1} if the size difference of the two events is not less than about one magnitude unit.

By simulating the spectral ratio of S and Lg waves within a certain group velocity window or first several seconds of P waves in each pair, we estimated the corner frequencies of 28 larger events in the pairs and plotted the estimated corner frequencies with the body wave magnitude m_b of these 28 events (Figure 3). As shown in the plot and as expected, the corner frequencies for these events decrease as the size of the earthquakes increase. We need to note that the earthquakes we studied here all have size larger than

magnitude 3 except one event. The corner frequency relation with event size here does not conflict with our previous result (*Shi et al.*, 1998) from earthquakes in Northeastern U.S. that, for intraplate earthquakes, the corner frequency of the event does not depend on the event size when the earthquake is less than about magnitude 3, and the corner frequency decreases with increasing event size for larger events.

From our experience, the trade-off between corner frequency and attenuation quality factor Q is the main problem in measuring the two parameters in quality factor, Q_0 and η. By using empirical Green's function deconvolution method in corner frequency estimate, we measured the source corner frequency from the source spectrum first before introducing the corner frequency measurement into the attenuation estimation process. The trade-offs are then sufficiently eliminated. Figure 4 shows two examples in the simulation of the source and attenuation spectrum model with the S and Lg displacement spectrum to find the best fit two path-averaged attenuation parameters Q_0 and η. From each spectrum, we estimate an event - station path-averaged Q_0 and η and obtain the spatial variation of attenuation in the region we analyzed.

Since only 28 events have their source corner frequency well estimated from empirical Green's function analysis, we obtain the event-station values of Q_0 and η for 28 paths based on the displacement spectrum of S and Lg waves within the group velocity range from 3.6 to 3.0 km/s. The path dependent values of these two parameters are plotted in Figure 5a and 5b. The degree of the background shade represents the elevation in the region, with mountains showing whiter.

It is very obvious that, for the quality factor Q_0, the values from the paths which

cross the Tien Shan mountains southwestern of WMQ are lowest, about 500 to 600. For the paths along the Tien Shan mountains to the west of WMQ, the Q_0 values are relatively higher, about 700. For the paths through the basin to the southeast of WMQ, Q_0 values are also relatively higher, about 800 - 900. There is only one path that crosses through the Tien Shan on east side of WMQ, and Q_0 seems lower than the path values of other groups, about 500. Generally, in each region, Q_0 from S and Lg waves on different paths are found to be consistent for regions of similar topography.

The variation of η for different paths seems not so much structure related (as is the case with Q_0), but is more randomly variable.

DISCUSSION AND CONCLUSIONS

We have analyzed Lg spectra from 28 earthquakes in XinJiang, China, with body-wave magnitude m_b ranging between 2.7 to 5.1. The empirical Green's function method was used to determine the source corner frequencies, and the spectral fitting of Lg displacement spectra was used to determine the path averaged Q_0 and η (Lg Q at 1 Hz and its power-law frequency dependent parameter, respectively). This method efficiently eliminated the trade-off between source corner frequency and attenuation quality factor Q in the estimate.

The Tien Shan is situated north of the Tarim basin, consisting of approximately east-west-trending blocks which are often separated by wide latitudinal valleys (*Ni, 1978*). Abundant evidence for thrust faulting throughout the present Tien Shan indicates that the

present range was built by crustal shortening and crustal thickening. It is one of the most seismically active mountain chains in the world, with lateral variations related to Cenozoic crustal shortening (*Burov et al., 1990; Li, 1990*). Hence, the geological structure near WMQ is quite complex as shown by *Feng* (1985), and *Patton et al.* (1985). We will expect the spatial variation in attenuation corresponding with this structure will also be complex. In order to see the correlation of the attenuation we obtained with the local structure, we contoured the values of Q_0 based on the path averaged Q_0 information from *S* and *Lg* waves (Figure 6). The region we analyzed can be considered as three groups, one group along the high elevated Tien Shan, another group cross the Tien Shan suture zone to southwest of WMQ, and one within the relatively lower elevated basin region to the southeast of WMQ.

The spatial inhomogeneity in attenuation near Urumqi is clearly correlated with the tectonic structure and path direction in the region. For the waves propagating along the Tien Shan mountains west of WMQ and south into the basin region which do not cross the thrust fault zone shown by *Tapponnier* (1979) and *Feng* (1985), the quality factor Q is relatively higher, and there is relatively lower attenuation. While for the seismic waves propagating across the Tien Shan mountains to the southwest which cross the thrust fault zone, we found the quality factor Q is relatively lower.

The attenuation we measured is an apparent attenuation which includes both intrinsic and scattering phenomena within the upper crust in the area. The quality factor Q at different frequencies is actually the total effect from intrinsic and scattering attenuation based on the scale of the structure at various frequencies.

ACKNOWLEDGMENTS

REFERENCES

Aki, K., Scaling law of seismic spectrum, *J. Geophys. Res.*, **72**, 1217-1231, 1967.

Atkinson, G. M., and R. F. Mereu, The shape of ground motion attenuation curves in southeastern Canada, BSSA, Vol. 82, No. 5, 2014 - 2031, 1992.

Burov, E. V., M. G. Kogan, H. Lyon-Caen, and P. Molnar, Gravity anomalies, the deep structure, and dynamic processes beneath the Tien Shan, *Earth Planet. Sci. Lett.*, **96**, 367-383, 1990.

Campillo, M., *Lg* wave propagation in a laterally varying crust and the distribution of the apparent quality factor in central France, *J. Geophys. Res.*, **92**, 12604-12614, 1987.

Chun, K.-Y., G. G. West, R. J. Kokoski, and C. Samson, A novel technique for measuring Lg attenuation: results from eastern Canada between 1 to 10 Hz, *Bull. Seism. Soc. Am.*, **77**, 398-419, 1987.

Feng, Xianyue, Seismogeological characteristics of the Xinjiang area, Seismology and Geology, Vol. 7, No. 2, 1985.

Gao, L, and P. G. Richards, Lower crustal and Upper-most mantle structure beneath station WMQ, China by teleseismic *P*-wave polarization signals, F49620-94-1-0057

report, 1995.

Li, Y., An apparent polar wander path from the Tarim Block, China, *Tectonophysics*, **181**, 31-41, 1990.

Mitchell, B. J., Frequency dependence of shear wave internal friction in the continental crust of eastern North America, *J. Geophys. Res.*, **85**, 5212-5218, 1980.

Ni, J., Contemporary tectonics in the Tien Shan region. *Earth Planet. Sci. Lett.*, **41**, 347-354, 1978.

Patton, H. J., S. R. Taylor, D. B. Harris and J. M. Mills (Jr.), The utility of regional Chinese seismograms for source and path studies in central Asia, Geophys. J. R. astr. Soc., 81, 469 - 478, 1985.

Shi, J., W. Kim, and P. G. Richards, Variability of crustal attenuation in the Northeastern United States from *Lg* waves, *J. Geophys. Res.*, **101**, 25231-25242, 1996.

Shi, J., W. Kim, and P. G. Richards, Correction to "Variability of crustal attenuation in the Northeastern United States from *Lg* waves", *J. Geophys. Res.*, **102**, 11899-11899, 1997.

Shi, J., W. Y. Kim, and P. G. Richards, The corner frequencies and stress drops of intraplate earthquakes in the Northeastern United States, *Bull. Seism. Soc. Am.*, *in press*, 1998.

Singh, S. and R. B. Herrmann, Regionalization of crustal coda Q in the continental United States, *J. Geophys. Res.*, **88**, 527-538, 1983.

Tapponnier, Paul, and Peter Molnar, Active faulting and Cenozoic tectonics of the Tien Shan, *J. Geophys. Res.*, **84**, 3425-3459, 1979.

FIGURE CAPTIONS

Figure 1. An example of event pairs in January 9, 1989 (m_b = 3.8 and 2.8) recorded by same station WMQ. The amplitude of the smaller event (*OT: 01/09/1989 15:22:01*) is almost 10 times smaller than the larger event (*OT: 01/09/1989 15:10:23*) but with similar wave forms.

Figure 2. Examples showing the spectral ratio (*thin lines*) of two event pairs from *Lg* waves within a group velocity window from 3.0 to 3.66 km/s and *P* waves of first 2.0 seconds after first *P* arrival. The thick smooth curve is the synthetic source function ratio in the frequency domain with estimated corner frequency information from optimization method. The solid arrow shows the position of the corner frequencies of the larger event (f_{c1}) and the smaller event (f_{c2}). If f_{c2} is not estimated, we fixed f_{c2} = 40 Hz and use an empty arrow to show it.

Figure 3. Two examples of the displacement spectra from which we estimated the attenuation information, Q_0 and η, with calculated corner frequency information. The arrows represent the position of the corner frequency of the event.

Figure 4. Plot of corner frequency with m_b magnitude of the larger events of the pairs. The squares represent corner frequencies from the *P* wave spectral ratio. The triangles represent corner frequencies estimated from the *Lg* wave spectral ratio.

Figure 5a. Q_0 values for all the 28 event-station paths we analyzed from *Lg* waves.

Figure 5b. η values for the event-station paths.

Figure 6. Attenuation quality factor Q_0 contours with the background topography

in the region. The density of the shade shows the elevation in the region, with whiter shade being higher elevated.

Table The event pairs selected from earthquakes in XinJiang.

No.	date			origin time			lat. (°N)	lon. (°E)	depth (km)	m_b	$f_c(P)$ (Hz)	$f_c(S)$ (Hz)
	y	m	d	h	m	s						
1	1988	01	13	14	05	23.4	41.717	88.550	-	3.3	10.0	-
	1988	01	27	18	33	27.9	41.700	88.567	-	2.6		
2	1988	03	04	12	03	0.9	41.883	88.433	-	4.0	4.5	4.5
a	1988	02	15	03	11	20.1	41.933	88.750	-	2.7		
b	1988	06	05	10	13	49.8	41.833	88.433	-	2.5		
3	1988	04	06	21	15	23.8	42.567	85.833	14.	2.7	9.0	8.0
	1988	01	05	14	14	37.3	42.617	85.850	-	2.6		
4	1988	07	04	00	54	34.2	43.683	87.967	28.	4.6	3.25	2.5
	1988	07	04	01	01	24.2	43.683	87.967	26.	3.4		
5	1988	08	03	23	51	47.	43.633	85.350	9.0	3.2	-	11.5
	1988	12	30	20	41	38.2	43.633	85.333	12.	2.5		
6	1988	08	09	02	51	23.9	43.783	86.533	15.	3.3	-	6.0
	1989	11	07	12	51	31.1	43.700	86.617	15.	2.5		
7	1988	09	03	03	50	8.9	43.333	85.350	18.	3.6	3.25	3.0
	1989	04	26	05	47	54.9	43.017	85.367	18.	2.6		
8	1988	09	18	06	39	11.0	41.983	88.683	11.	3.6	6.75	6.0
a	1989	11	28	08	37	25.4	41.983	88.800	16.	2.8		
b	1989	03	01	16	57	9.9	42.050	88.550	11.	2.7		
9	1988	09	24	11	12	38.3	43.367	88.783	13.	3.7	6.5	-
	1989	04	19	04	46	12.6	43.717	88.583	13.	2.5		
10	1988	10	05	17	10	22.9	42.417	85.850	23.	3.4	4.875	3.875
a	1989	06	26	20	43	56.0	42.367	86.033	17.	2.6		
b	1988	01	05	14	14	37.3	42.617	85.850	-	2.6		
c	1988	04	06	21	15	23.8	42.567	85.833	14.	2.7		
11	1988	10	06	06	01	2.2	42.583	85.733	26.	3.2	8.75	8.25
a	1989	12	21	16	22	43.9	42.600	85.933	16.	2.5		
b	1988	10	10	17	26	24.3	42.567	85.800	18.	2.6		
12	1988	11	01	20	24	16.0	42.917	87.933	2.	3.5	5.0	6.5
	1989	11	19	07	14	49.7	43.050	87.783	5.	2.7		
13	1988	11	14	18	42	13.1	42.050	88.200	3.	3.2	8.0	8.0
	1988	11	28	15	25	11.3	42.050	88.133	13.	2.5		
14	1988	11	15	16	56	45.3	42.217	89.333	11.	5.1	2.33	1.67
a	1988	11	15	16	54	49.5	42.200	89.400	11.	2.5		
b	1989	07	23	15	42	14.7	42.183	89.350	17.	2.6		
15	1988	12	07	05	58	0.6	41.867	88.450	15.	3.6	-	4.0
	1989	06	07	18	12	51.0	41.983	88.450	20.	2.8		
16	1989	01	09	15	05	16.3	42.700	88.283	15.	4.5	3.5	3.9
	1989	01	09	15	21	45.9	42.683	88.267	12.	2.8		
17	1989	01	09	15	10	14.5	42.450	88.217	-	3.8	5.0	5.0
	1989	01	09	15	21	45.9	42.683	88.267	2.	2.8		
18	1989	01	09	18	51	13.4	42.017	85.833	6.	3.5	-	5.5
	1988	04	11	18	36	49.3	42.100	85.783	8.	2.5		
19	1989	01	12	01	35	45.9	43.067	87.217	-	3.8	3.875	3.75
a	1989	08	27	17	32	5.7	43.033	87.800	7.	3.0		
b	1989	11	19	07	14	49.7	43.050	87.783	5.	2.7		
c	1989	05	25	18	08	42.6	43.133	87.300	13.	3.1		
20	1989	02	27	15	07	1.1	42.967	85.233	6.	3.2	7.5	6.0
	1988	11	08	15	42	22.4	42.950	85.483	3.	2.6		
21	1989	05	09	10	37	11.3	43.733	86.233	23.	3.5	3.25	2.5
a	1989	03	07	23	04	21.2	43.733	86.217	29.	3.0		

No.	date y	m	d	origin time h	m	s	lat. (°N)	lon. (°E)	depth (km)	m_b	$f_c(P)$ (Hz)	$f_c(S)$ (Hz)
b	1989	07	29	17	34	40.8	43.717	86.183	30.	2.8		
c	1989	10	13	05	21	38.2	43.717	86.667	26.	2.6		
22	1989	05	25	00	47	5.8	42.317	88.100	21.	3.9	-	5.0
	1988	01	26	10	07	14.2	42.283	88.000	-	2.5		
23	1989	06	03	12	37	30.6	42.217	85.500	20.	3.6	3.5	3.5
	1988	03	19	16	06	43.8	42.633	85.500	-	2.5		
24	1989	06	17	03	18	56.3	42.333	85.333	7.	3.4	-	4.5
	1988	03	19	16	06	43.8	42.633	85.500	-	2.5		
25	1989	08	13	18	47	21.9	42.450	87.817	22.	4.4	4.75	2.75
	1989	05	24	19	29	22.3	42.433	87.667	14.	2.5		
26	1989	08	29	20	39	20.1	42.400	85.900	14.	3.8	4.5	4.0
a	1989	06	26	20	43	56.0	42.367	86.033	17.	2.6		
b	1989	08	01	16	15	22.4	42.683	85.883	21.	2.6		
c	1989	07	12	18	47	34.2	42.583	85.883	20.	2.7		
27	1989	09	22	20	54	27.6	42.083	87.833	11.	3.1	5.5	5.0
a	1989	06	05	16	27	19.2	42.033	87.883	11.	2.5		
b	1988	02	19	07	36	52.8	42.033	87.850	-	2.5		
28	1989	11	25	23	40	55.2	43.750	86.200	28.	3.5	4.5	4.0
	1989	12	17	22	37	24.0	43.800	86.100	26.	2.5		

Note,

The first event in each pair is the larger event, and the smaller ones are the possible

pair event to the larger event. Some event may have more than one possible pair, and the

corner frequencies we estimated are the average of values derived by deconvolution of all
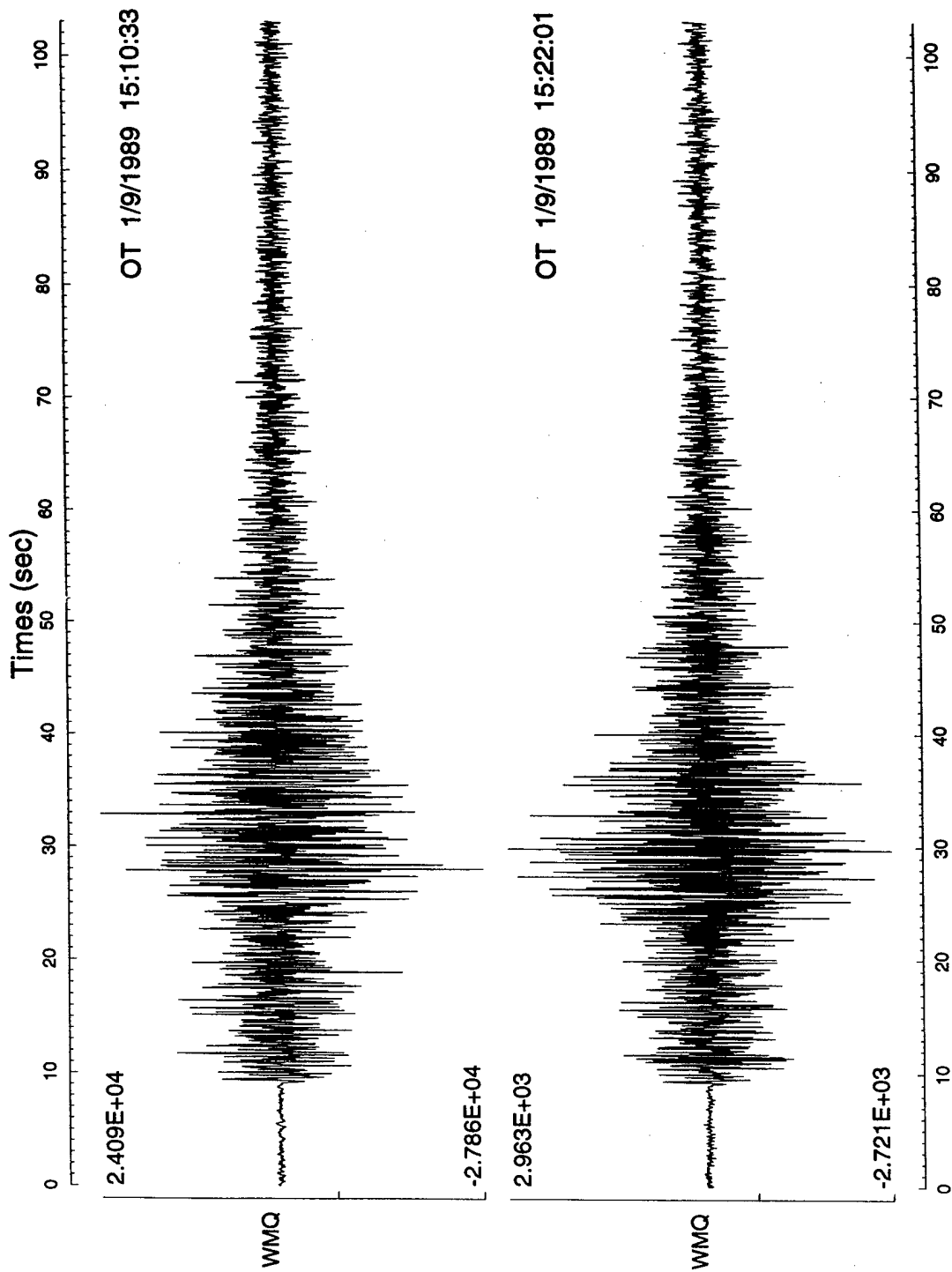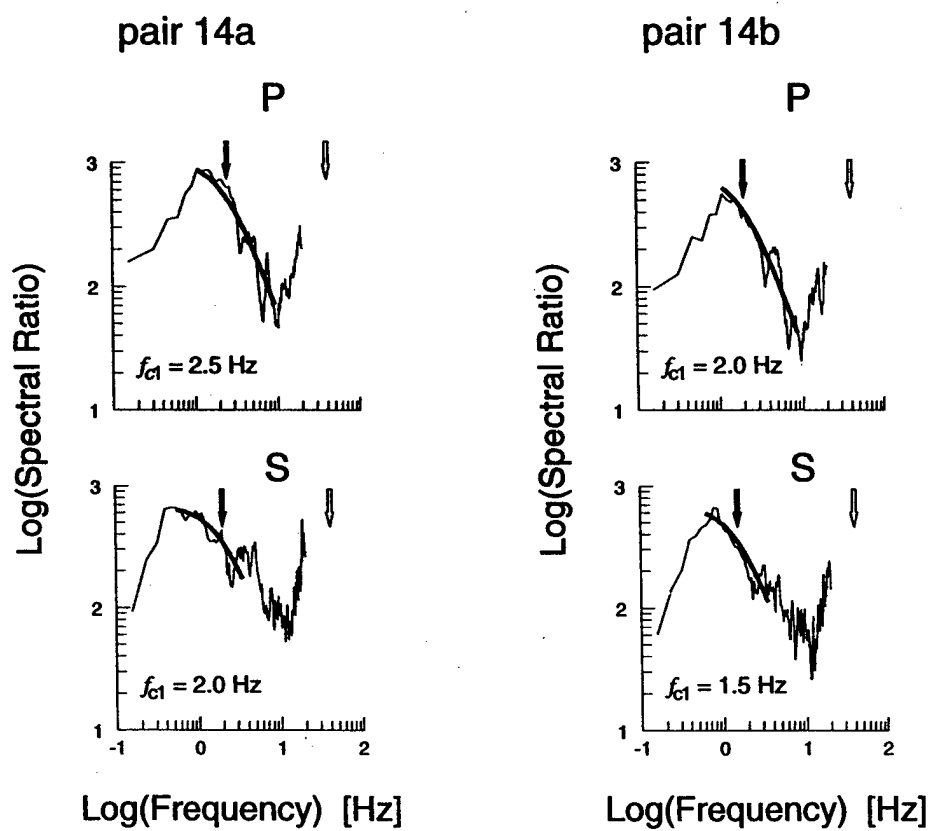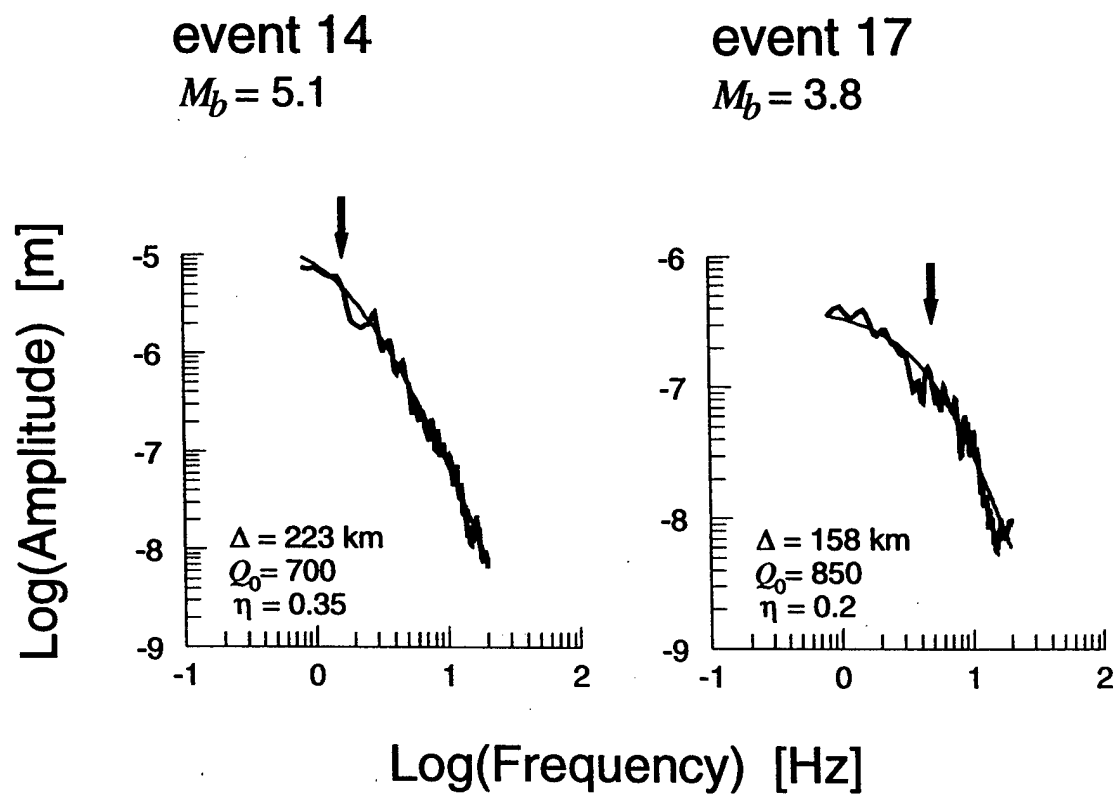
possible pairs.

181

Fig. 1

pair 14a

pair 14b

P

P

S

S

$f_{c1} = 2.5$ Hz

$f_{c1} = 2.0$ Hz

$f_{c1} = 2.0$ Hz

$f_{c1} = 1.5$ Hz

Log(Spectral Ratio)

Log(Frequency) [Hz]

Log(Frequency) [Hz]

Fig. 2

Fig. 3
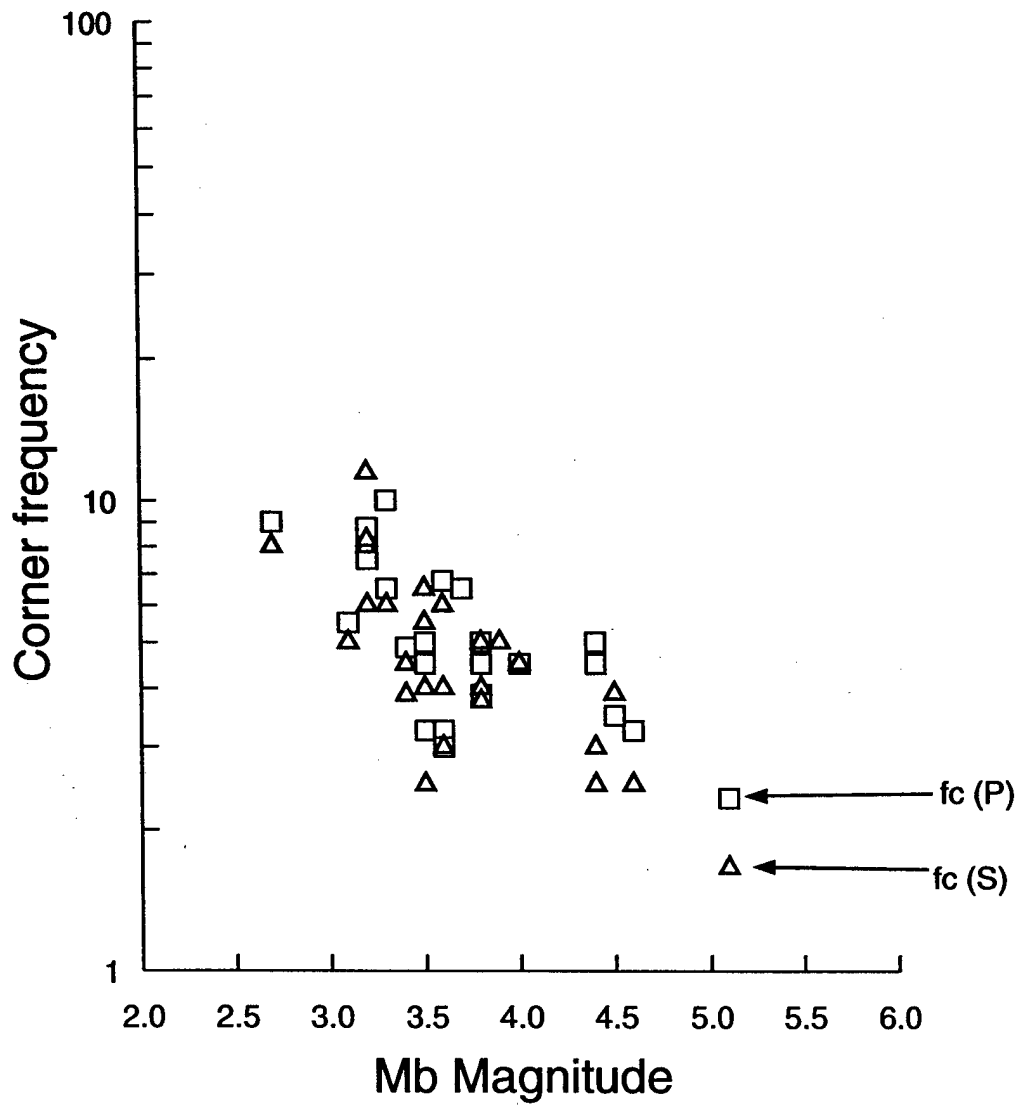
Fig. 4

Path-averaged Q_0
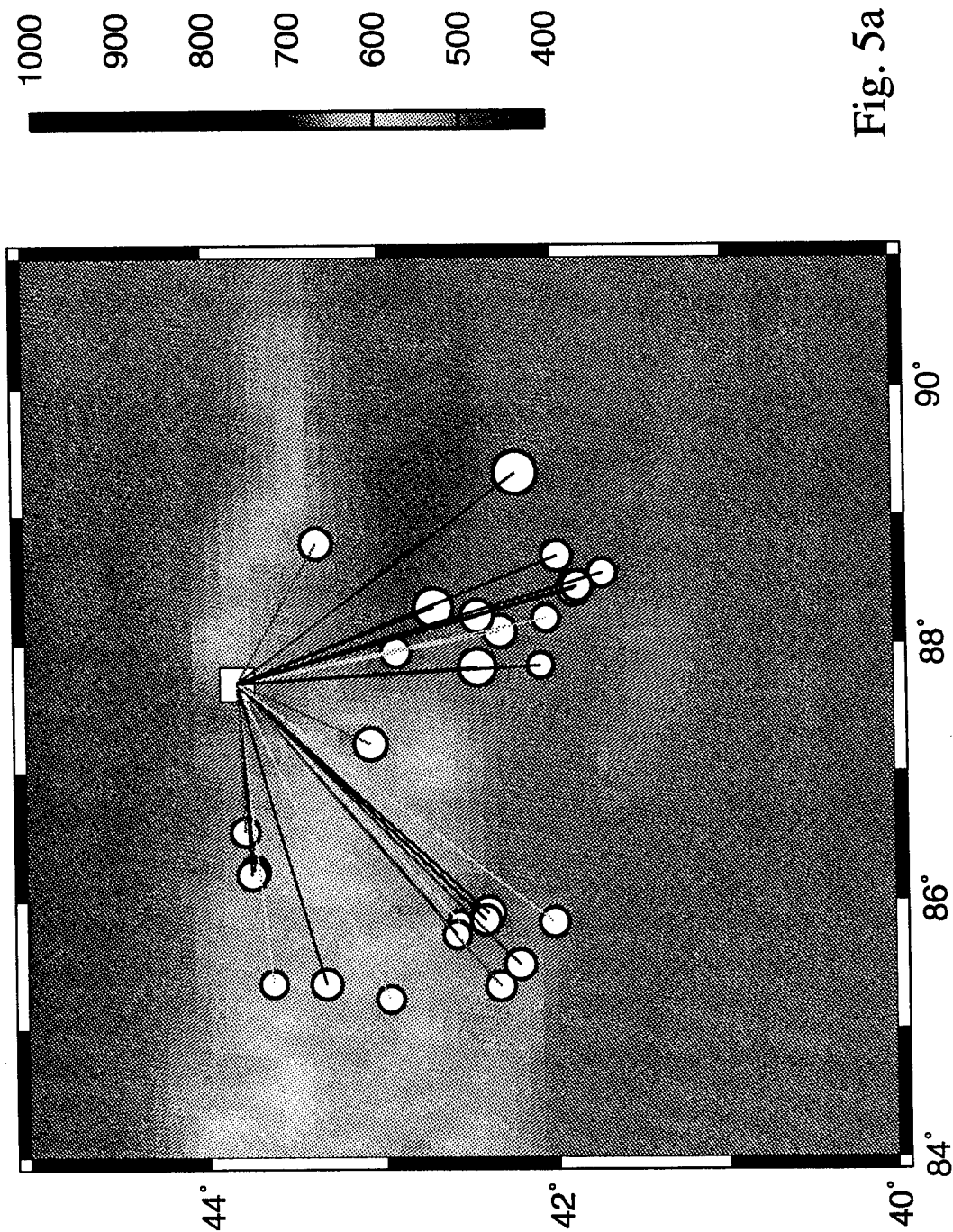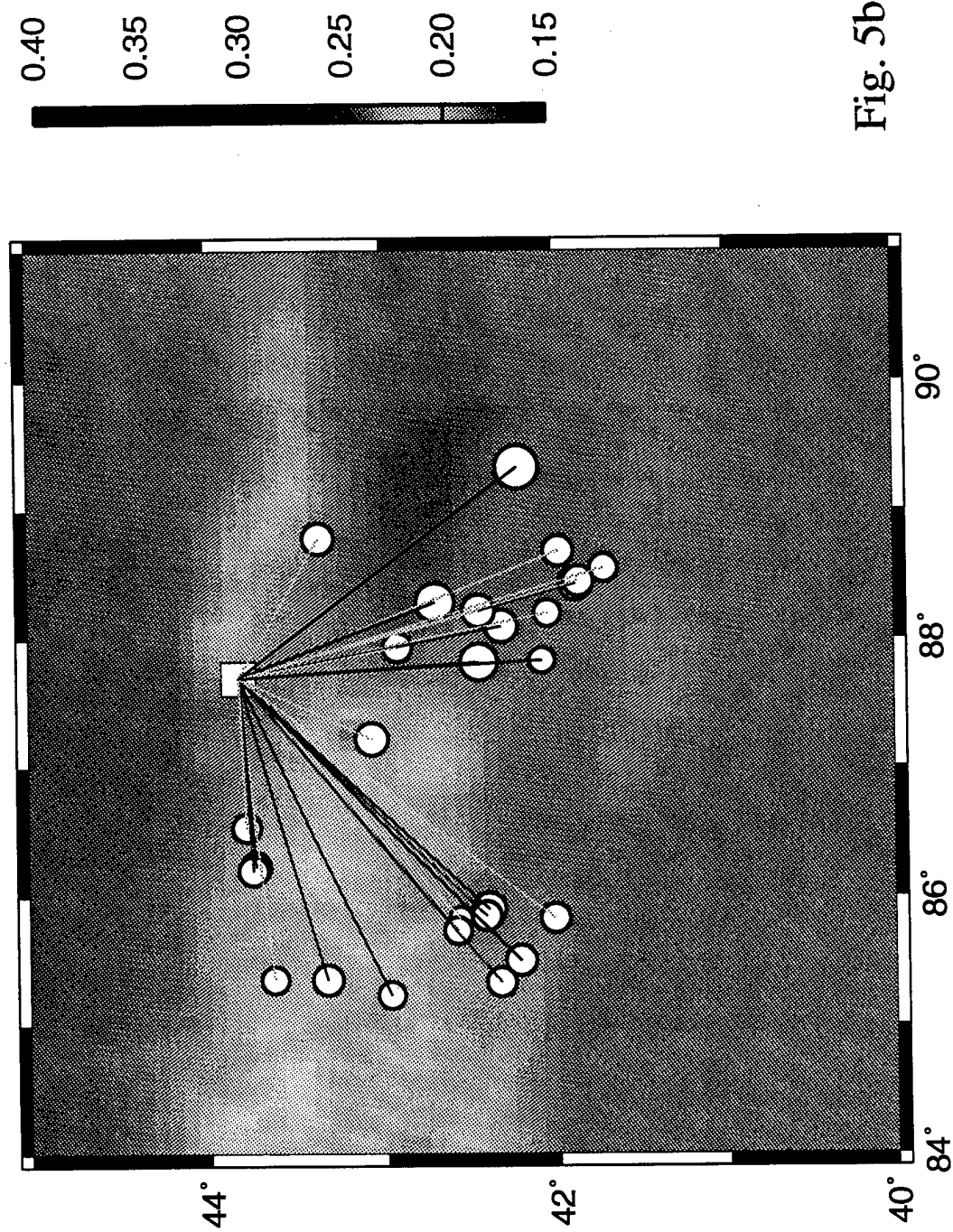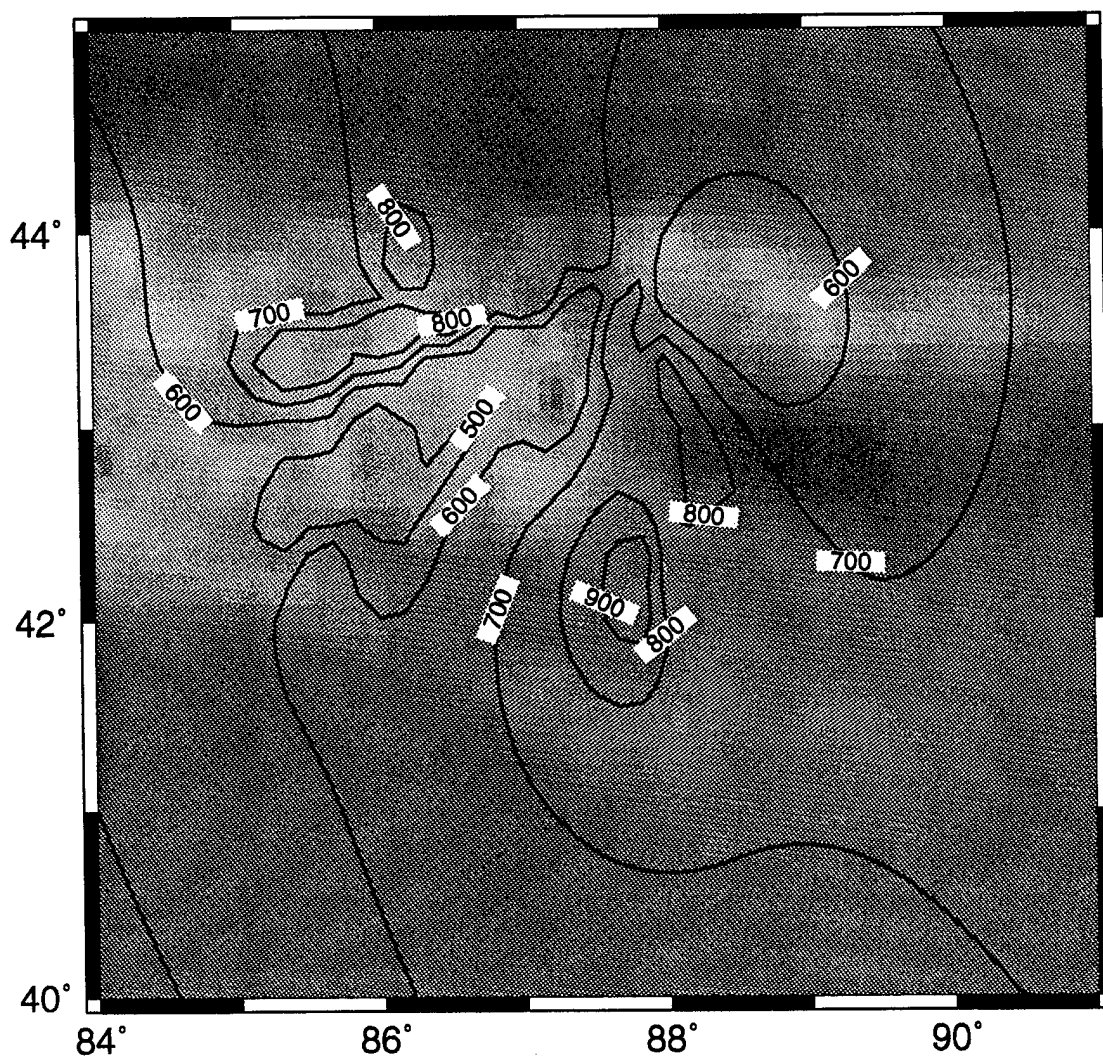
Fig. 5a

Path-averaged η

Fig. 5b

Q_0 contours

Fig. 6

Part 3. Description of an unusual swarm of seismic activity in Western China

The Lop Nor test site, like the Nevada test site of the United States, lies in an area of active tectonics, and thus will be associated with numerous seismic events that may be detected and are likely to require analysis in a CTBT monitoring program. This section of the present report describes an unusual swarm of seismic activity that is a subset of the Lop Nor seismicity described in a previous report under our grant from AFOSR. The swarm consisted of more than 400 small seismic events in a period of about 100 days, beginning on December 27, 1975, and centered in Western China at (44.25°N, 85.65°E). It is not clear whether the swarm was a natural phenomenon, or whether it was due to human activity (such as mine blasting).

To give the context, Figures 1 through 5 of this part of the final report show the location of 2757 seismic events reported by the Chinese State Seismological Bureau, for the years 1970 and 1972 through 1989, for the region between latitudes 37°N and 45°N, and between longitudes 85°E and 93°E. Figure 1 shows the location of all the 2757 events, which have magnitude 2 and above (the full set of events), together with a rectangle close to (41.5°N, 88.5°E) indicating the location of the Lop Nor nuclear test site. Figure 2 shows the same data set for the 884 events of magnitude 3 and larger; Figure 3 is for the 164 events of magnitude 4 and larger; Figure 4 is for the 31 events of magnitude 5 and larger; and Figure 5 is for the 4 events of magnitude 6 and larger.

When the events for 1975 and 1976 are examined for their distribution in time, in space, and in magnitude, as shown in Figures 6 and 7, it is apparent that several hundred events are strongly clustered in time and space, beginning on December 27, 1975, and ending about one hundred days later. These 434 events are all within 20 km of the point (44.25°N, 85.65°E), and about 300 km Northwest of the Lop Nor test site.

Figure 8 shows on an expanded scale the location of the 434 events occurring in the swarm from Dec 27, 1975, to April 4, 1976. It is apparent that the State Seismological Bureau reports event locations to the nearest 1/60 of a degree (i.e., to the nearest minute), so the locations are discretized and many of the points shown represent multiple events. The Times Atlas shows an East-West road running at about latitude 44.2°N through the points in this Figure, and to the town of Manass off the Figure to the East at (44.20°N, 86.14°E).

Figure 9 shows the number of events reported per day. There is no particular pattern, as for example might expected for mine activity (for which a weekly periodicity is common, some mines choosing to blast mainly on weekends, and other mines avoiding weekends). Figure 10 shows the events occurring per half-hour of local time-of-day, for the 100-day duration of the swarm, and again there appears to be no simple pattern such as a dominance of events during daylight working hours (very common for mining activity and construction blasting).

It is common for an earthquake to be followed by a sequence of smaller events. In such cases the sequence begins with a large event (the "main shock"), followed by aftershocks of general decreasing magnitude and frequency. Figure 11 shows how the 434 events are distributed in magnitude and time. Such a pattern is absent in this figure. The sequence simply ends in early

April, as shown also in Fig. 7. For a swarm of earthquakes associated with volcanic activity, there is typically no dominant event that starts the sequence—which tends to have a gradual beginning and ending.

Figure 12 shows how the 434 events are distributed in magnitude. In this plot of N(M) against M, N(M) is the cumulative number of events in the cluster with magnitude M or greater. A line given by $\log N(M) = 5.4 - 1.4 M$ is a good fit to the data. A slope closer to the value -1 would be more typical of a natural aftershock sequence.

The swarm is unusual in that it does not display the characteristics of either a natural earthquake sequence, or human activity such as blasting associated with a construction project or mining. It is presumably one or other of these alternatives. Possibly, the sequence continued but a decision was made not include the events following April 4, 1976 in the State Seismological Bureau catalog. Figures 6 and 7 indicate that only for the duration of the swarm, were events reported that had magnitude lower than 2.5. Since the daily rate often reached around 10 or 20 events, and occasionally even more (see Fig. 9), mine- or construction-blasting seems unlikely. It cannot, however, be ruled out. If a swarm this large raised questions in the context of CTBT monitoring, the nature of the swarm could perhaps best be resolved by non-seismic methods.
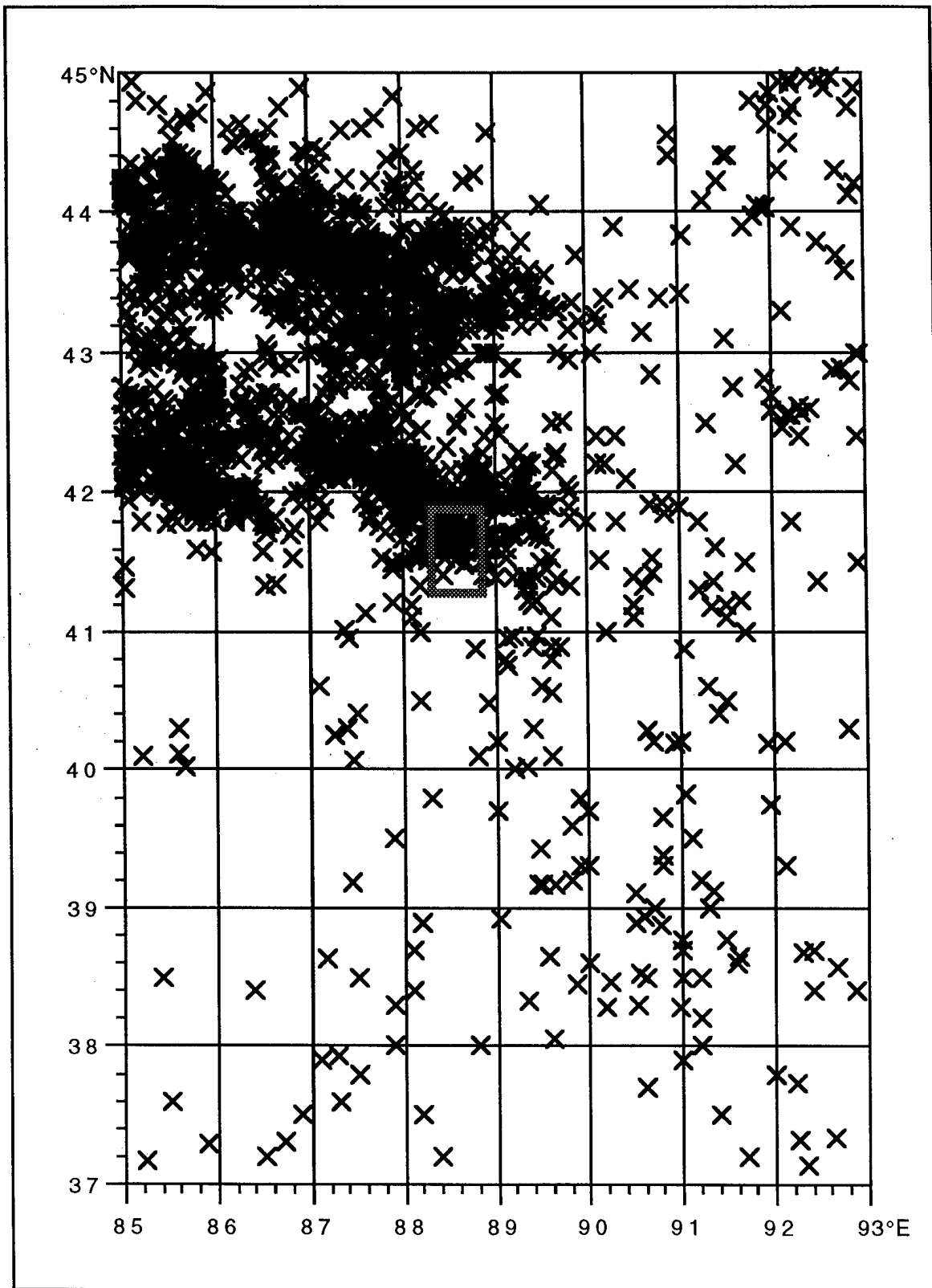
Figure 1. The location of all 2757 seismic events for the 19-year period 1970, and 1971 – 1989, reported by the Chinese State Seismological Bureau for the rectangle from 37°–45°N, 85°–93°E. The location of the Lop Nor test site is shown as the rectangle 41.3°–41.8°N, 88.3°–88.8°E.
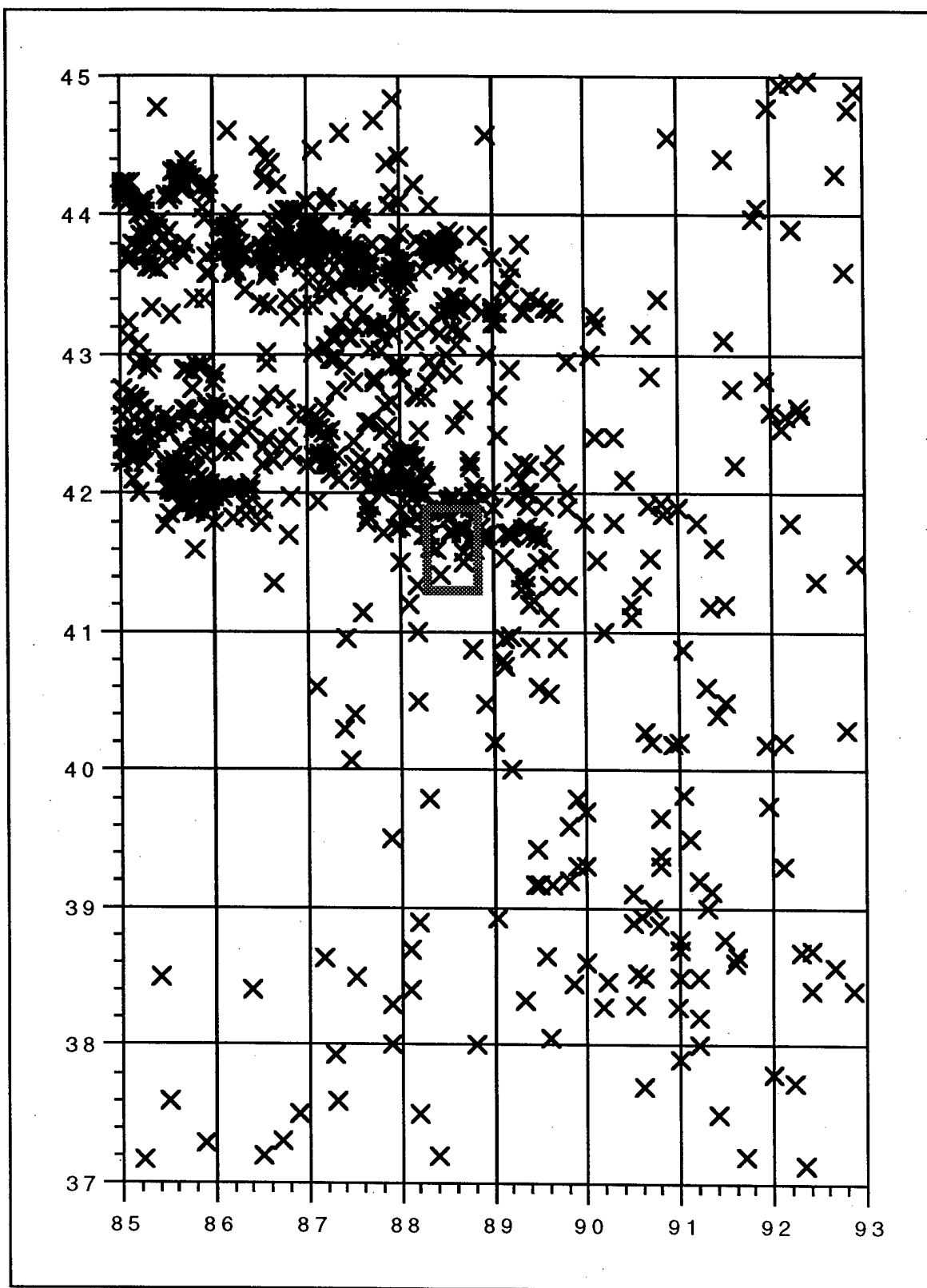
Figure 2. Same as Fig. 1, but showing the 884 events with magnitude 3 and larger. Note a concentration of events near (44.25°N, 85.65°E). These events clustered in time as well as space.
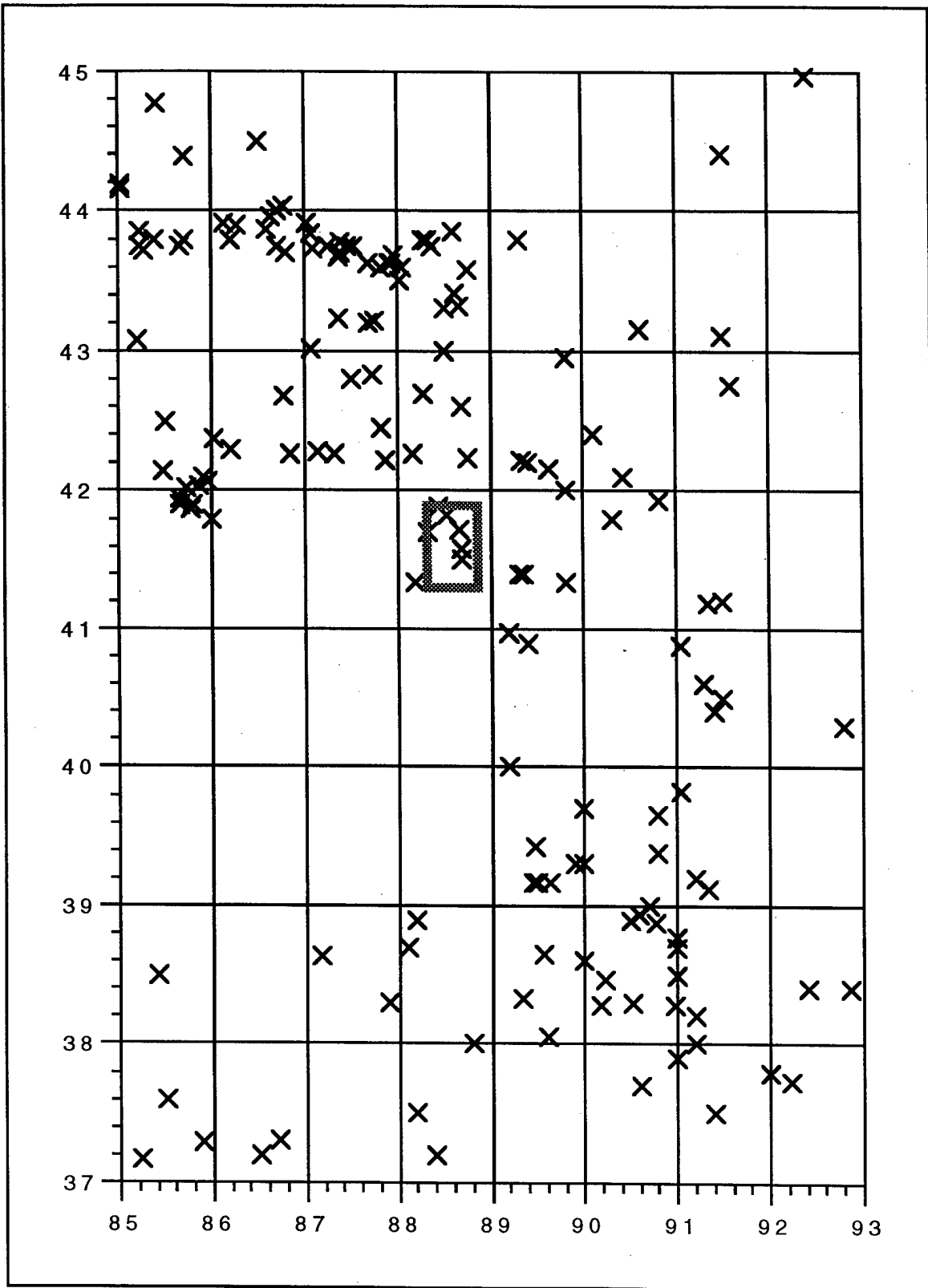
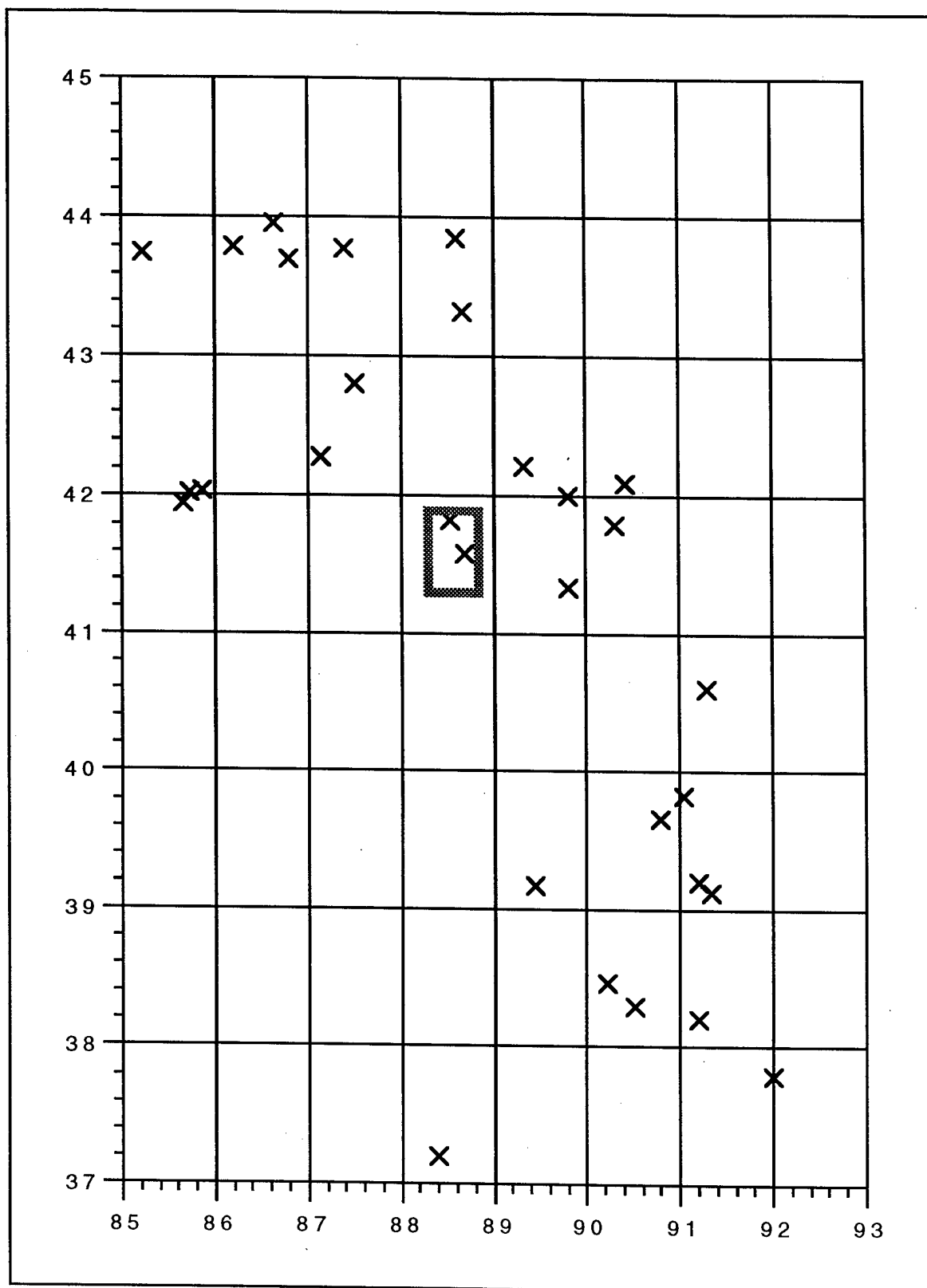Figure 3. Same as Fig.1, but showing the 164 events with magnitude 4 and larger.

Figure 4. Same as Fig.1, but showing the 31 events with magnitude 5 and larger.

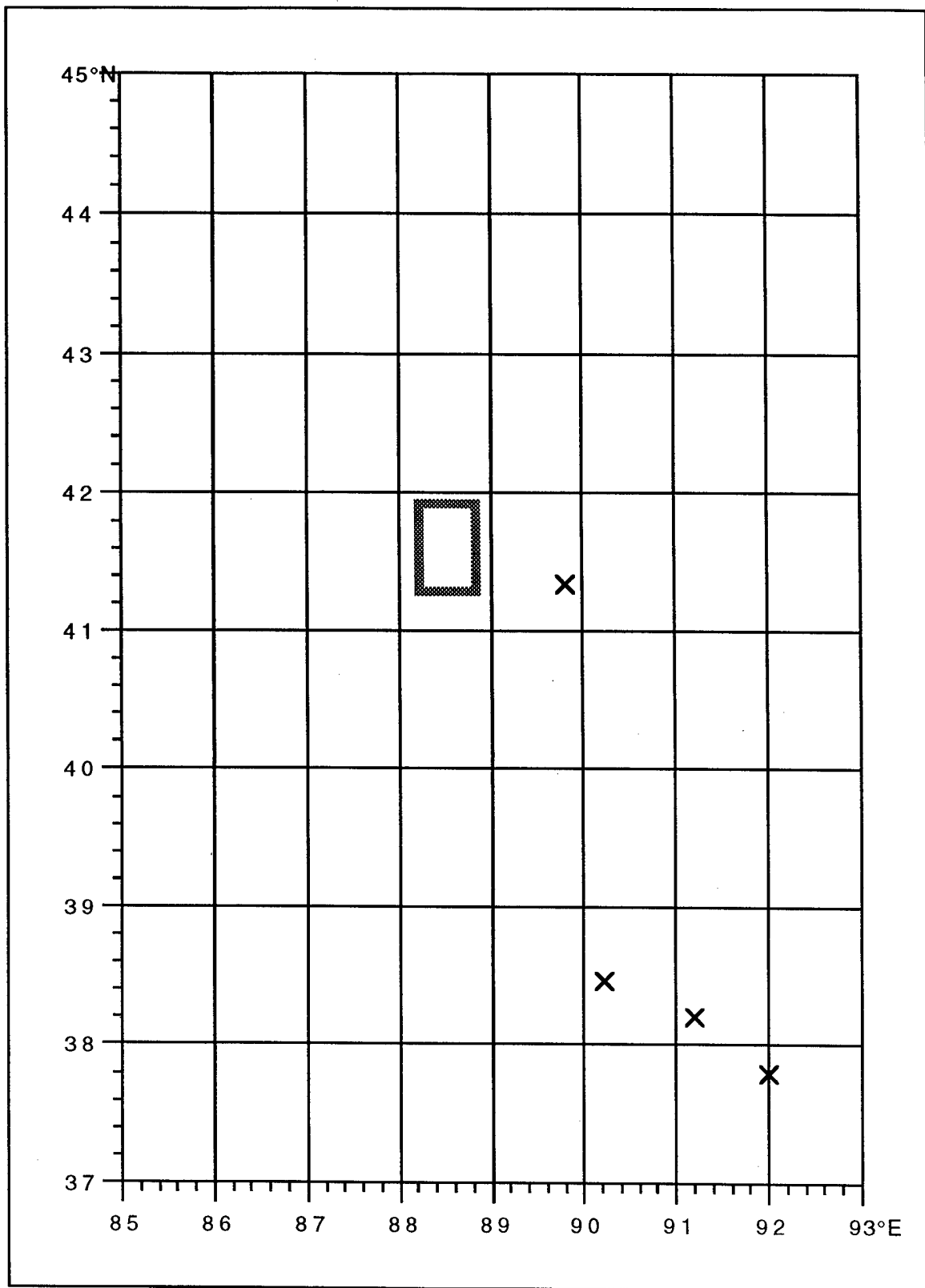Figure 5. Same as Fig.1, but showing the 4 events with magnitude 6 and larger.
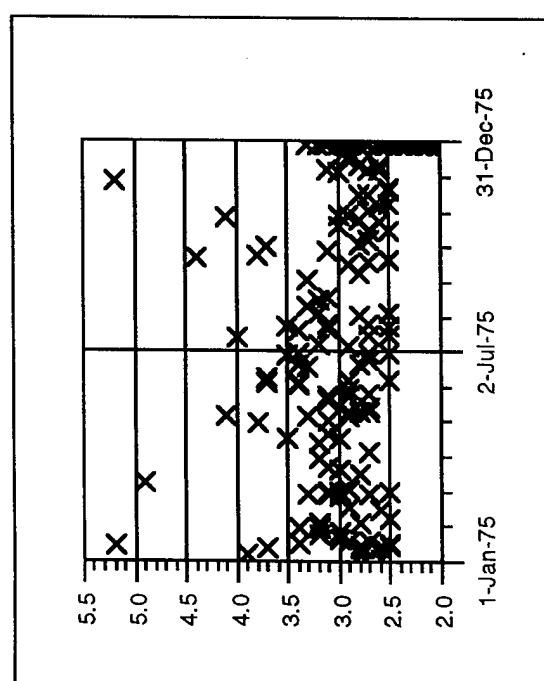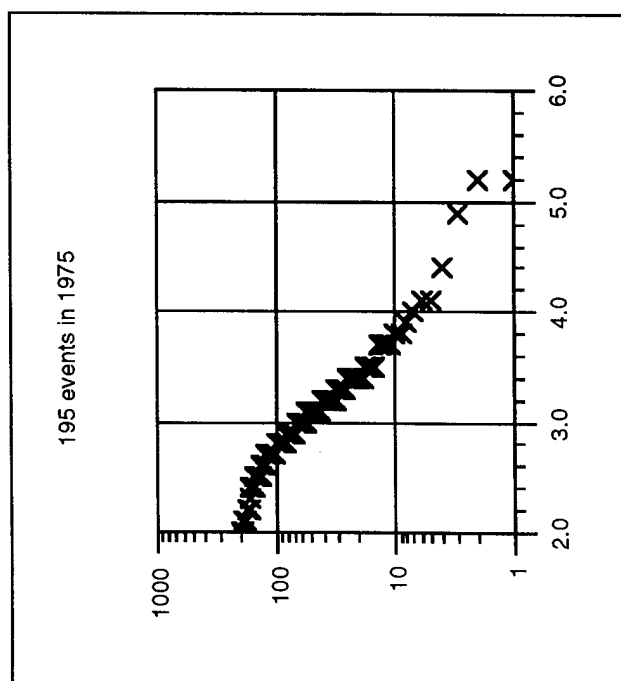
Figure 6. Distribution of seismicity in the Lop Nor region, with respect to magnitude, time, and space, for the year 1975
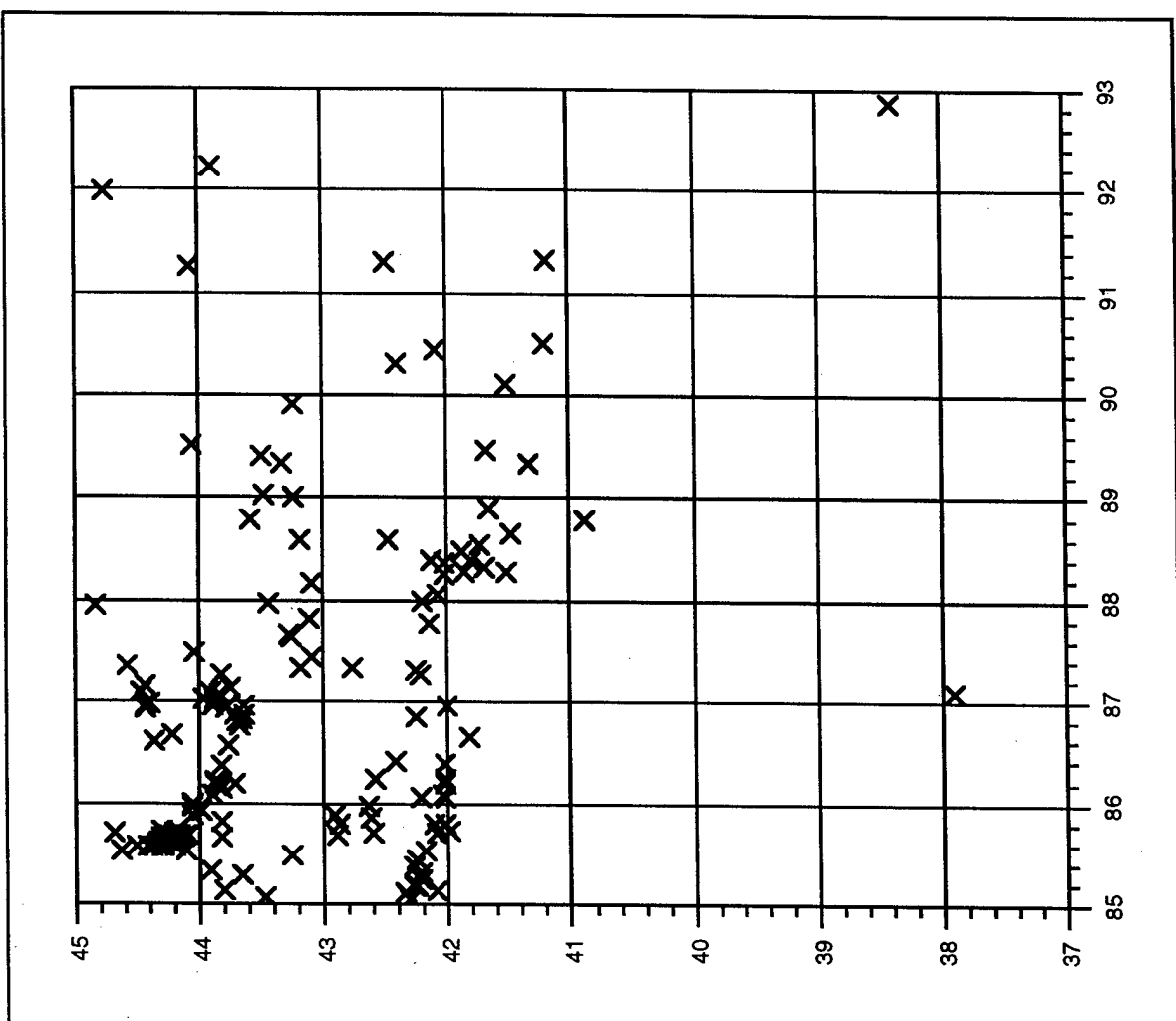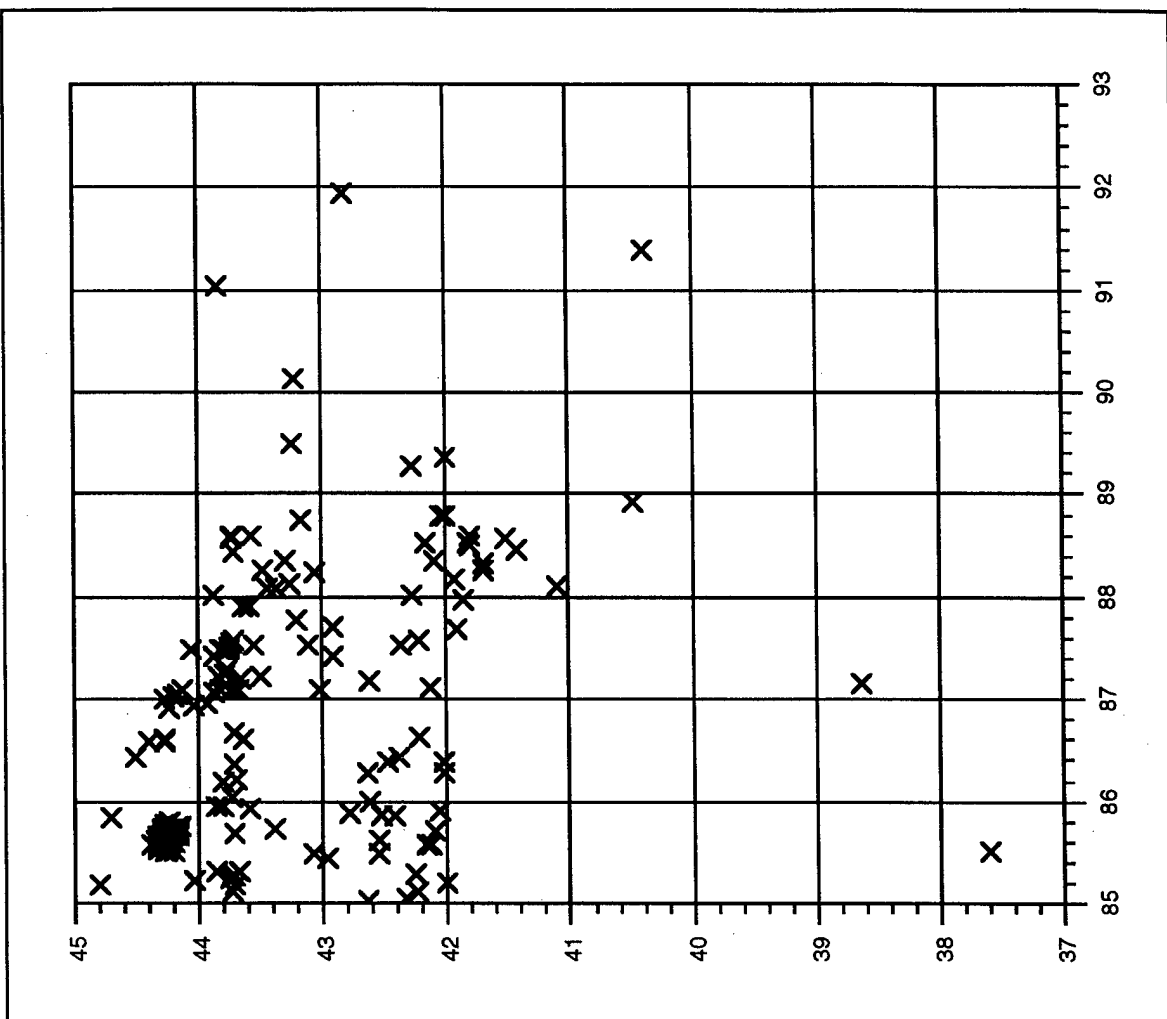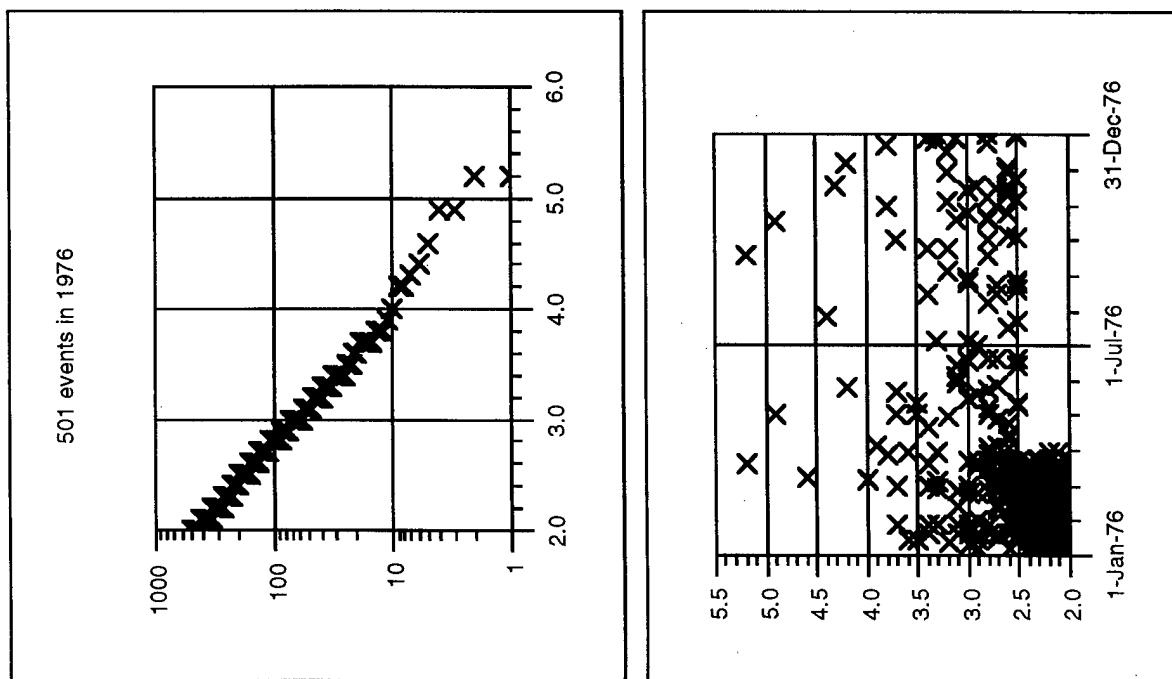
Figure 7. Distribution of seismicity in the Lop Nor region, with respect to magnitude, time, and space, for the year 1976
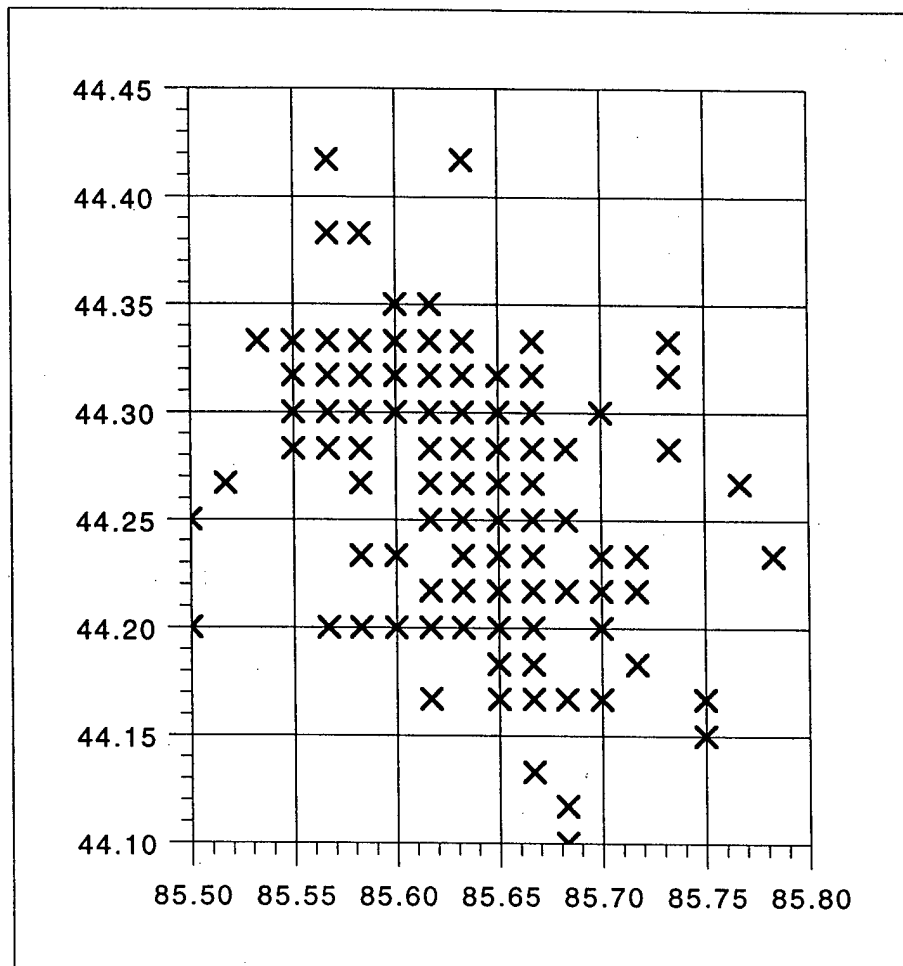
Figure 8. Map of locations near (44.25°N, 85.65°E) of 434 clustered events in W. China.
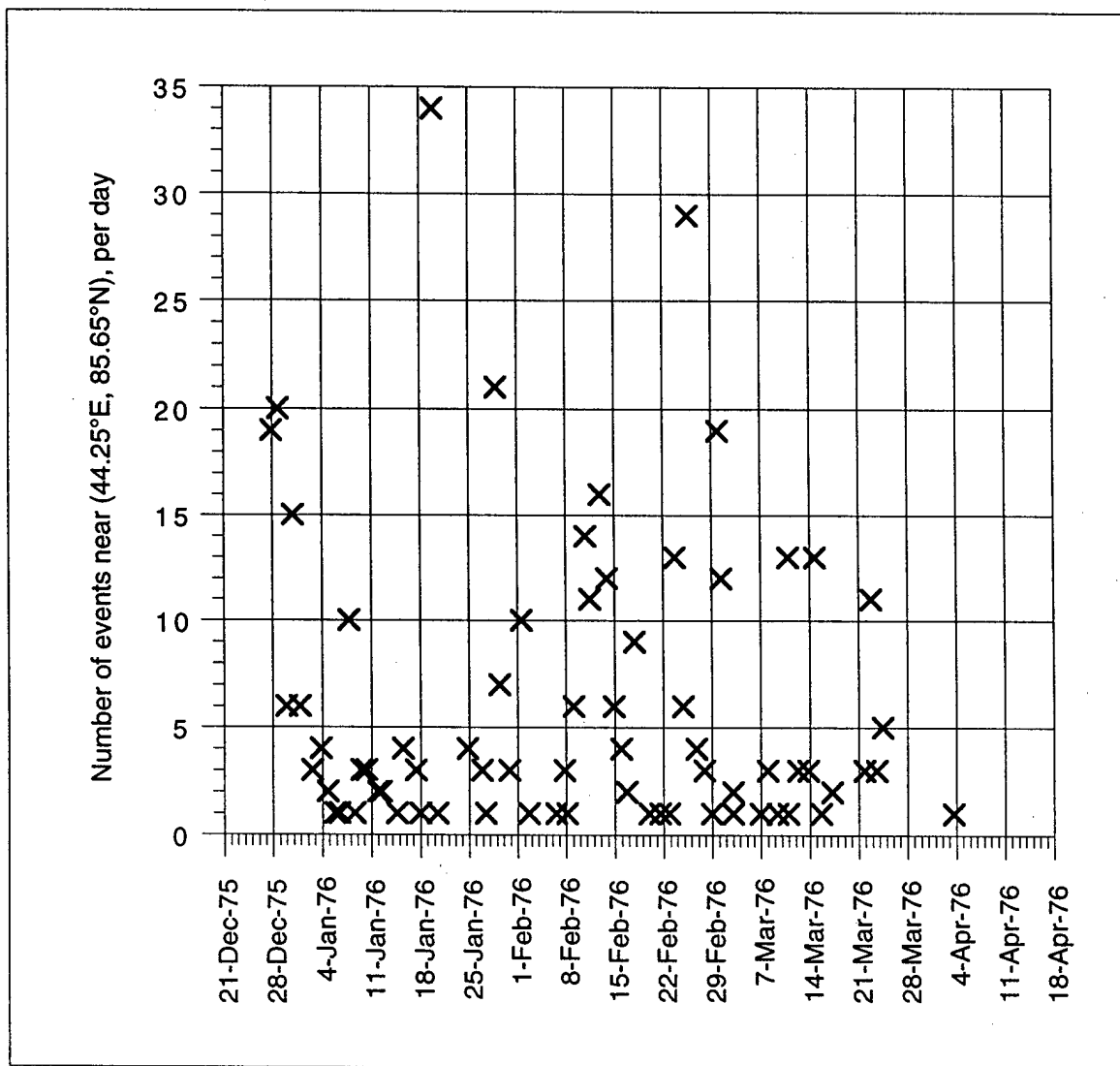
Figure 9. The number of events per day is shown for each day of the sequence. No weekly periodicity is apparent.
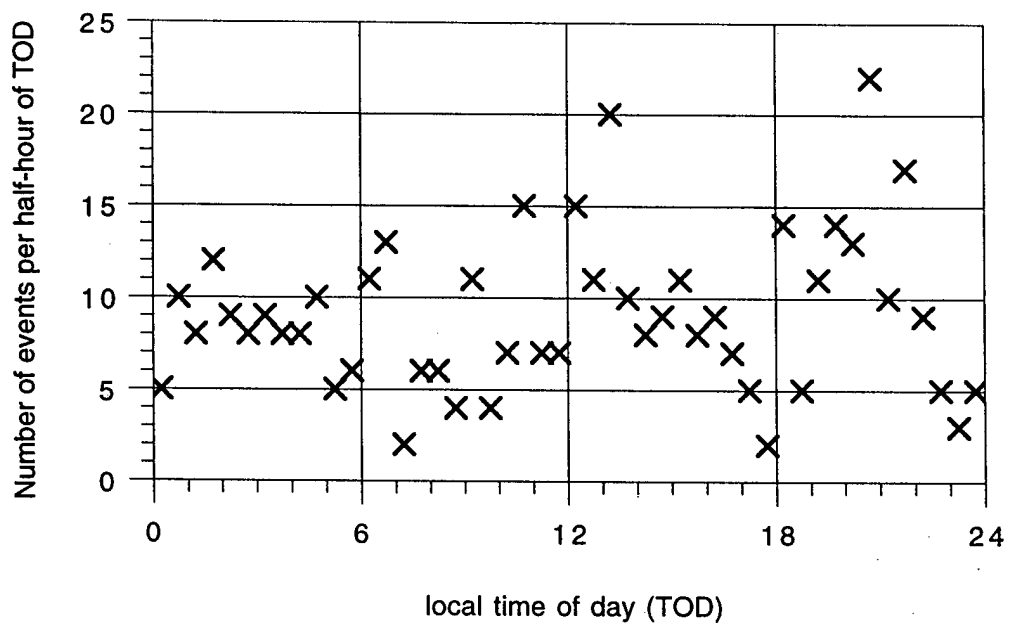
Figure 10. The number of events per half-hour is shown as a function of local time-of day. No pattern is apparent, such as occurrence during daylight hours or the usual working hours.
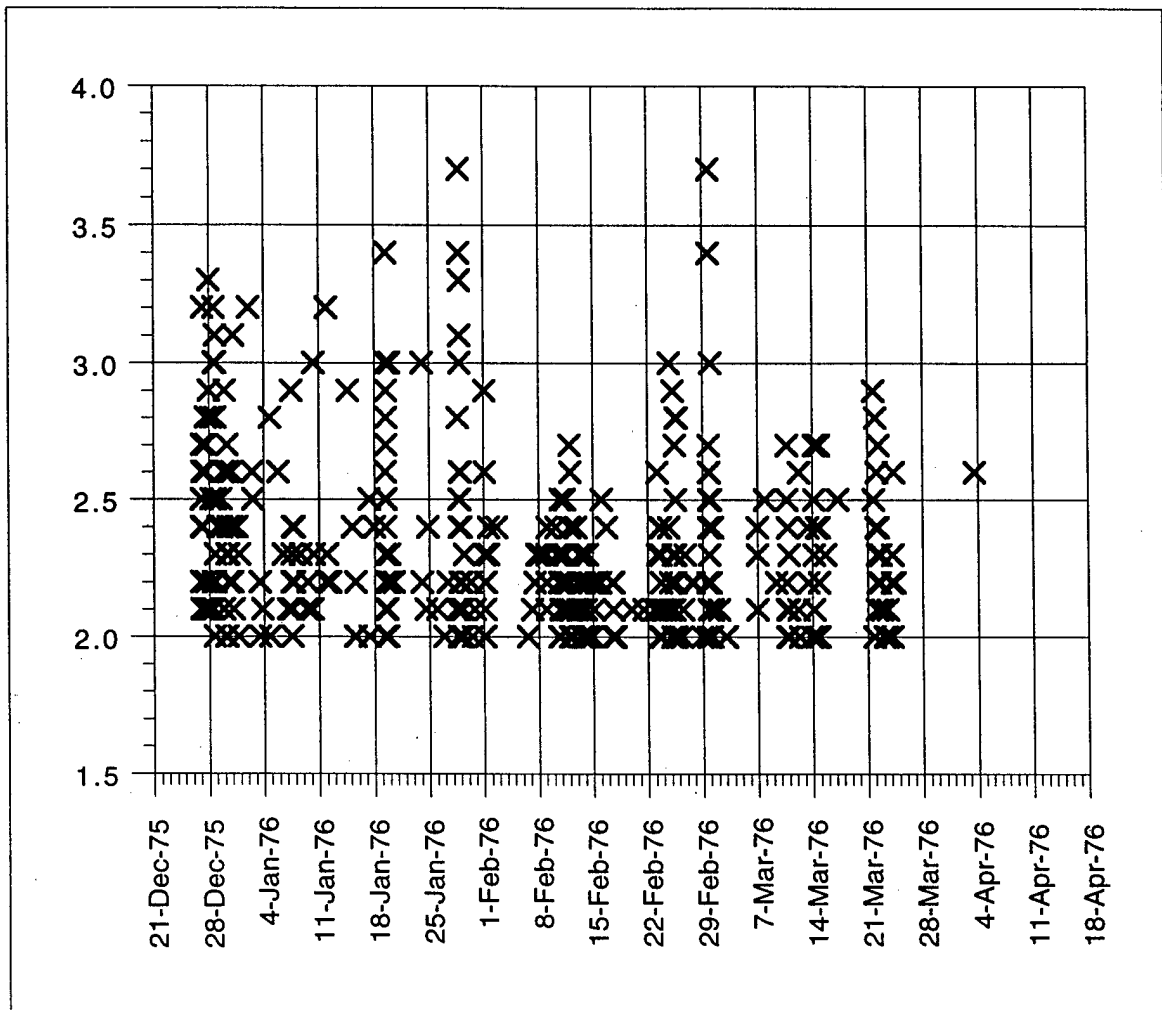
Figure 11. Each of the 434 events is plotted as a function of its magnitude and time of occurrence.

cluster, W. China; 100 days; log N(M) = 5.4 – 1.4 M
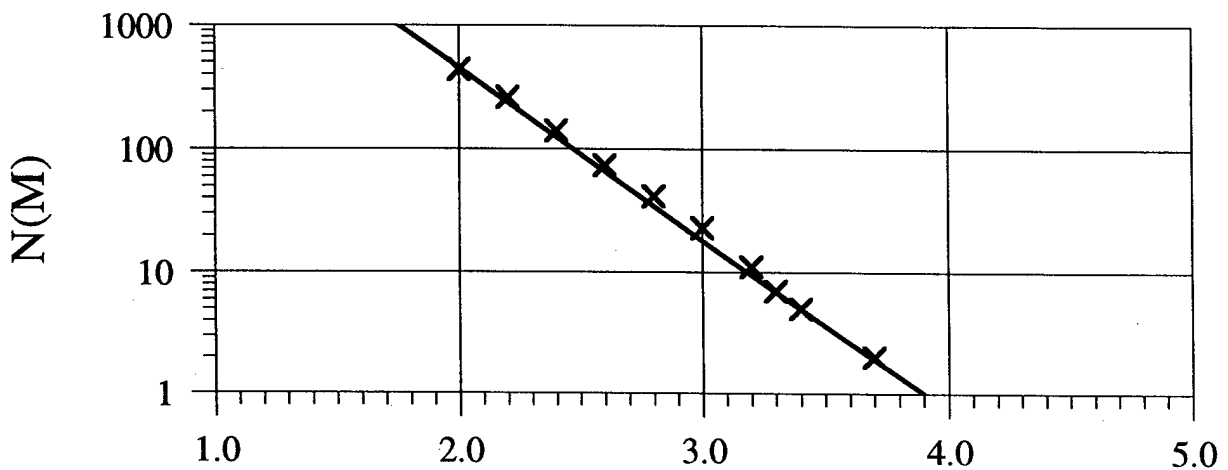
M; near (44.25°N, 85.65°E); 27 Dec '75 to 4 Apr '76

Figure 12. The cumulative magnitude, N = N(M) = number of events with magnitude ≥ M, is shown to fit a straight line of the form   log N(M) = 5.4 – 1.4 M. Such a line is common for earthquake activity, but not for a cluster of short duration that does not begin with a main shock of larger magnitude.

Part 4. A stand-alone paper entitled

Upper Mantle Structure Beneath Western China Studied with the Cross-array in Kazakstan

W.-Y. Kim, J. Xu[1] and P. G. Richards[1]

Lamont-Doherty Earth Observatory of Columbia University,
Palisades, NY 10964, USA
[1] also Department of Earth and Environmental Sciences,
Columbia University

ABSTRACT

The use of seismic arrays to determine slowness and travel time greatly enhances the identification of later arrival branches of the P-wave travel time curve between 12° and 30°. The cross-array in Kurchatov, Kazakstan is a medium aperture array with a total aperture length of 22.5 km. It has provided high-quality digital records and is well located for a detailed investigation of travel times and slownesses of P-wave branches at distances around 20° underneath most parts of central Asia. In this paper, over 100 earthquakes and an underground nuclear explosion which occurred in the Tibet Plateau and western China during 1995–1996 were used to study the upper mantle velocity structure. Events which have occurred in the distance range 10° – 32° and with event-to-station azimuth range of 312° – 339° from the Kurchatov array are selected for analysis. A simple weighted, delay-and-sum beam-forming method was used to determine the travel times, slownesses and azimuths of the first arrival P as well as later arrival P phases. The travel time and slowness data are corrected for focal depth and local structure, and are used to invert for the upper mantle P-wave velocity structure. The results of the inversion for one dimensional velocity structure indicate the existence of several discontinuities including known discontinuities at depth of 417 km and 690 km. A preliminary result is that a sharp increase in P velocity between about 550 to 600 km depth is indicated by the later-arrival P phases. The data provide resolution of velocity structure down to about 780 km depth.

Introduction

With the advent of digital seismometry and recent advances in microprocessor and communication technologies, there is an upsurge of interest in seismic arrays. Approximately 22 to 30 seismic arrays[1] are being considered for deployment in the next few years as primary network stations of the International Monitoring System (IMS) for monitoring the Comprehensive Test Ban Treaty. Availability of the seismic data from these IMS seismic arrays deployed at various places worldwide will certainly stimulate the use of seismic array data for various seismological investigations. The cross-array in Kurchatov, Kazakstan is a such regional medium aperture array. Figure 1 shows the cross-array location and its configuration. The large territory of the central Asian Republic of Kazakstan, located in the stable interior of Asia, is uniquely suited for sensitive monitoring of global seismicity, and nuclear explosions. The great distance from major oceans, low levels of cultural and seismic activity, and the excellent transmission characteristics of the exposed rock of the Kazakh platform provide locations for low-noise, low-attenuation recording sites. In October of 1994, a centralized digital recording system was installed to record the short period seismometers of an existing 21-element cross-array at Kurchatov city on the former East Kazakstan nuclear test site. The cross-array has two orthogonal linear arms, each consisting of 11 boreholes (average depth ≈ 45 m) containing short-period, vertical-component seismometers with station spacing of 2.25 km (Kim *et al.*, 1996). The total aperture length is about 22.5 km. The instrument response of the borehole seismograph is nearly flat to input ground velocity in the frequency band 0.5 – 5 Hz and signals are recorded continuously with a sampling rate of 40 samples/sec. The cross-array has provided high-quality digital records since its operation and is well located for a detailed investigation of travel times and slownesses of *P*-wave branches at distances around 20° underneath most of the central Asia.

The most direct information on the *P*-wave velocity distribution in the upper 800 km of the mantle comes from observations of refracted *P*-wave arrivals at epicentral distances of less than 30°. Two general properties of the velocity structure of the upper mantle—a zone of low or negative velocity gradient above 250 km (the *low-velocity zone*), and regions of high velocity gradient between 300 and 700 km (the *transition zone*)—are now accepted. However, regional models differ significantly in detail. The differences may be caused by variations in structure, but difficulties in the interpretation of the observed data are also involved.

In this paper, beam-forming was used in a relatively small time window (usually 1.2 to 2 seconds) to determine the slownesses and travel times not only for the first arrival but also for the later arrivals. Based on these measurements, we derive an initial upper mantle *P* velocity structure

---

[1] ANNEX 1 to the Protocol, Comprehensive Nuclear Test-Ban Treaty, September 10, 1996, listed 22 seismic arrays, and eight additional stations which will each be deployed as a three-component station to be upgraded to an array at a later date.

in western China using the Herglotz-Wiechert inversion technique, which uses distance as a function of $dT/d\Delta$. We then modify the initial model by comparing the predicted travel time and the observations.

Data

The region studied is one of the most complex areas of present day tectonic activity. It appears impossible to find a one-dimension model to fit all data from a wide range of sources. But in a narrow azimuth range such as shown in the Figure 2, it is possible to find a one-dimension model to fit the observations for a good range of distances. We selected approximately 100 events which have occurred in western China during 1995 and the first four months in 1996. The epicentral distances of the selected events extend from 10° to beyond 30° in the azimuth range 312° to 339° (from the event to the cross-array) to cover this narrow area. The events are listed in Table 1 and the locations of epicenters are shown in Figure 2.

A seismic record section of the waveforms from earthquakes in the distance range 10° to 20° is shown in Figure 3. The waveforms recorded at the center of the array (C21; Figure 1) are plotted with a reduction velocity of 10 km/s (= 11.12 s/deg). The record at a distance around 11.5° is from an underground nuclear explosion on 08/17/95 (00:59) at the Lop Nor Chinese test site. In Figure 3, the predicted travel time curve calculated using the IASPEI 91 model for a focal depth of 15 km is plotted and various P-wave travel time branches are indicated (Kennett & Engdahl, 1991). For instance, the A–B branch represents Pn arrivals and the C–D branch represents first arrival P-waves whose rays have turning points below the 410 km discontinuity, whereas the branch G–H is a portion of the P travel time branch corresponding to rays turning below the 660 km discontinuity. A line joining C to B is the receding branch due to a zone of rapid velocity increase near the 410 km discontinuity. However, the data do not show a clear amplitude change at the edge of the receding branch at C in Figure 3 (distance range of 14°-16°), suggesting a less pronounced velocity change above the 410 km discontinuity in the study area. The record from each event is plotted without adjusting for its focal depth. Note that at certain distances there are multiple arrivals within a very short time window, as well as possible arrivals of depth phases generated near the source. These complex arrivals will lead to slownesses and travel times that are poorly determined for parts of particular travel time branches.

A synthetic record section calculated using the IASPEI 91 model for a focal depth of 15 km is shown in Figure 4 to help interpret the observed record section shown in Figure 3. The source mechanism from an event on 12/18/95 (04:57, M=5.7) is used to calculate amplitude and travel time using the WKBJ seismogram method (Chapman, 1978). The synthetics show essentially similar features for the first P waves when compared with the observed record section shown in

Figure 3. However, the synthetics show less complex later arrivals, since the depth phases are not included. Also simplifying the synthetics, the source time function used is a delta function convolved with an attenuation operator having t* = 0.1 s. Nevertheless the synthetic record section is a useful tool to interpret various later arrivals on the observed records.

Observations of Travel Time and Slowness

Analysis of Array Data

It has long been recognized that a considerable reduction of seismic noise is possible by beam-forming array data (Mykkeltveit *et al.*, 1990; among others). We employed a simple weighted, delay-and-sum (WDS) beamforming algorithm to process the cross-array data to measure the slowness, p, and arrival time, T, of the first P wave as well as several later arrival P waves at the center of the array (Capon *et al.*, 1967; Johson & Dudgeon, 1993). The array beam, $z(t)$, calculated for the array center located at (x_0, y_0) may be written as

$$z(t) = \sum_{m=1}^{M} w_m s_m(t - \delta t_m) \tag{1}$$

$$\delta t_m = (x_m - x_0) \cos \phi/c + (y_m - y_0) \sin \phi/c + \tau_m$$

where w_m = amplitude weight at the m-th sensor located at (x_m, y_m), $s_m(t)$ = record at the m-th sensor, δt_m = time delay, ϕ = direction of the arriving plane wave, c = propagation velocity of the plane wave (reciprocal of the horizontal slowness), and τ_m = station correction that may be applied. The essence of the method is that each record is shifted in time with respect to the reference record by the delay, so that the signal arrival time becomes common to all stations; and then a simple algebraic sum of all the records is computed at each instance. The delays compensate for the propagation delays and the waveforms at individual sensors add constructively. It is shown that the WDS yields nearly as much signal enhancement as other more elaborate array processing techniques such as adaptive array processing (e.g., King *et al.*, 1973; Filson, 1975; Johnson & Dudgeon, 1993). In equation (1), c, ϕ and τ_m are assumed to be known quantities. In practice, wave propagation velocity, c, and direction, ϕ, are found by calculating all beams in the expected slowness ranges, say, 0.07 to 0.125 s/km with a preset increment of approximately 0.001 s/km in both x and y directions, and then finding the c value that gives the clearest beam signal. In this study, usually over 1,000 beams are calculated for each time window and the best fit is found that yields maximum beam power, which is computed as the mean-squared amplitude. The observed data are pre-filtered with a third order Butterworth filter with cutoff frequencies at 1 and 5 Hz.

Usually about 15 sec of signals after the first arrival P-wave are analyzed. Beam-forming is performed using a 1 to 2 second time window depending upon the size of the event, since large

events tend to show longer period pulses due to source duration. We find strong beam power in several time positions which indicate the arrivals of signals when we move the beam-forming window along the time axis. The positions of high beam power accurately determine the arrivals of signals.

An example of array processing of the data is shown in Figure 5. The signal to noise ratio (SNR) is enhanced by the beam-forming technique, and the identification of the later arrivals is improved. In Figure 5a, the first trace is the reference station waveform, and the second trace shows the array beam calculated by using the slowness and azimuth determined from the small time window which is indicated by the short vertical lines. The apparent velocity, azimuth, and the maximum beam power determined from each small time window, are plotted in Figure 5b. When we move the time window along the time direction, we obtain the apparent velocity, azimuth and beam power at each specific time. This process allows us to identify clearly the first arrival as well as depth phases and other later arrivals. It is clear that when a signal arrives, the beam-power sharply increases from the background level, and the azimuth and slowness become stable. We can directly obtain the slowness and travel time values for the first and later arrivals by carefully comparing these figures (Figs. 5a through 5d).

First Arrivals

Usually we can pick up the first arrivals precisely. Studying them give us some important constraints on the later interpretation. Figure 6 shows the travel time and slowness of the first arrivals. Using the PDE location (Preliminary Determination of Epicenters, published by the U.S. Geological Survey) for the source, the arrival times and distances are corrected to surface focus. The measured slowness value ($1/c$) is used to determine the corrections for each arrival using the equations given by Bullen (1963, p. 104). For the sake of consistency with the initial model used in the velocity inversion in the later section, the IASPEI 91 velocity model has been used in determining these corrections. These corrections are about 4.2 sec and 0.13° for the travel time and distance, respectively, for a P arrival with a slowness of 0.1 s/km from an event with focal depth of 20 km, while for P arrivals with the same slowness from an event with depth of 10 km, these corrections are 2.1 sec and 0.06° for travel time and distance, respectively. Hence, even a moderate amount of error in the event focal depth will affect the correct interpretation of the travel time and slowness data. The focal depth is usually the least well constrained source location parameter in the PDE listings. For most of the events with unconstrained focal depth, conventionally listed in the PDE catalog as 33 km, we determined the focal depth using slowness of later arrival phases and we also adjusted the origin times of these events.

When the travel time and slowness data are presented separately, the relationship between

travel times and slownesses is not readily apparent, and resolution of finer features is lost in the scatter of the data. In Figure 6, a substantial improvement has been achieved by the incorporation of the travel time and slowness data in a single presentation following the method of Simpson *et al.* (1974). At each travel time point a line is drawn with the slope corresponding to the measured value of slowness reduced to a reference slowness of 0.1 s/deg. The length of the line is scaled to the weight given to the slowness determination and corresponds to ±0.5° for a well determined slowness. Part of the scatter in the data shown here can be attributed to errors in the PDE locations, in particular, errors in focal depth. The travel time and slowness data are also subjected to the effects of local structure beneath the array and to possible systematic bias due to errors in the travel time curve used to locate the events.

A careful inspection of Figure 6 reveals that the slope lines, which should lie tangent to the trend of the travel times at each point, show a bias away from the average curve. This bias is due to a shift in the measured values of slowness caused by local structure near the array. If a knowledge of the structure causing these variations is available, it is possible to compute corrections to the measured slowness value (Niazi, 1966; Zengeni, 1970). Niazi has shown that the effect of dipping layers beneath an array is to change the measured values of slowness by a factor which remains essentially constant over limited ranges of azimuth and slowness. Simpson *et al.* (1974) used this method in analyzing the WRA (Warramunga, Australia) array data. We applied this method to the Kurchatov cross-array with events in a narrow azimuth range. At each distance where a slowness determination was available, the slope of the smoothed curve was compared with the measured value of slowness. The rms residual was computed and the procedure was repeated with all measured first arrival slowness values multiplied by a factor ranging from 1.2 to 0.9. A minimum in the rms residual occurs with a correction factor of 1.06, indicating that the observed slowness values are low by about 6%. The travel times with slowness values corrected for local structure are shown in Figure 6, which shows the improvement in the trend of the slope lines with respect to the travel time curve, especially between 20° and 24°. The abrupt changes in slowness in the first arrival data of Figure 6b indicate that there are at least three major first arrival branches with cross-over points at 19° and 25°.

Later Arrivals

Based on the previous work, we can pick up not only the first arrival but also the later arrivals in the improved waveform. All data are corrected for event depth and local structure. Figure 7 show the slowness distribution, and the size of the circles represent the quality of the slowness measurement. Even though the scatter in the data cannot give us clear choices of slowness change, we can still recognize that there exist several branches in order to fit the distribution.

Velocity Structure

Herglotz-Wiechert Inversion

If the source and the receiver are both at the Earth's surface, the angular distance $\Delta(p)$ between the source and the point at which the ray with parameter p emerges can be written as (see, e.g., Aki and Richards, 1980)

$$\Delta(p) = 2\,p \int_{r_p}^{r_0} \frac{1}{\sqrt{(r/v)^2 - p^2}}\, \frac{dr}{r} \tag{2}$$

where p is the ray parameter, $p = r \sin i / v(r)$, r_0 is the Earth's radius, r_p is the radial distance to the deepest point of the ray and $v = v(r)$ is the velocity as a function of radius. The corresponding travel time $T(p)$ is given by

$$T(p) = 2 \int_{r_p}^{r_0} \frac{(r/v)^2}{\sqrt{(r/v)^2 - p^2}}\, \frac{dr}{r} \tag{3}$$

The Herglotz and Wiechert (H–W) formula for the analytical inversion of (2) and (3) is

$$\ln\,[r_0/r(v)] = \frac{1}{\pi} \int_0^{\Delta(r/v)} \cosh^{-1}\,(pv/r)\, d\Delta \tag{4}$$

The inversion is applicable to cases in which the derivative of $\Delta(p)$ is discontinuous, but not to cases in which $\Delta(p)$ itself is discontinuous. Thus the Herglotz-Wiechert formula cannot be used in cases involving low-velocity zone (LVZ). However, Slichter (1932) found an upper bound for the thickness of low-velocity zone from observed gaps $\delta\Delta$ and δT in the travel time curve.

Once we have the $\Delta = \Delta(p)$ relationship, we can determine the velocity profile $v = v(r)$ and hence the one-dimension model can be obtained. It is difficult to fit the slowness data shown in Figure 7 using only one curve. We separate the slowness data to several branches which can be fitted by a set of polynomial curves. Because we do not yet have not enough data to determine the local crust model, we use the global IASPEI 91 crust model as the local model.

Upper Mantle Velocity Model for Western China

Unfortunately because of the scatter in the slowness measurement, the direct determination of velocity by H–W inversion of these data alone does not appear warranted. Using the model from H–W inversion as an initial model, together with trial and error, we determine a velocity model which explains the observed features and which does not produce features that are not warranted by the observed data. For example, the amplitude should provide important constraints

on the velocity model, such as the nature of the velocity discontinuities: the ends of the major prograde branches terminate with low amplitude, whereas high amplitudes are associated with the ends of retrograde branches.

The model W China that we obtained is shown in Figure 8 and is tabulated in Table 2. The model has two well known discontinuities at 417 km and 689 km. The model also shows a rapid increase in velocity between 550 to 600 km followed by low velocity gradients from 600 to 690 km. The travel times calculated from the W China model are compared with the observed waveform data in Figure 9.

Conclusion

The use of an array to determine slowness, and to associate later arrivals with particular branches of the P travel time curve between 10° and 32°, has revealed a number of consistent features. The most striking feature of the data is a pronounced later-arrival branch from 20° to 24° which we associate with an abrupt velocity increase near a depth of 550 km. Large-amplitude later arrivals are also observed around 15°, which indicate a region of high velocity gradient near 417 km. Both of these regions of high amplitude later arrivals are on the retrograde ends of the triplications resulting from velocity transitions near 417 km and 690 km. Although determinations of the exact depth and shapes of the velocity transitions are limited by the non-uniqueness of the inversion of the scatter in our data, we consider the main characteristics of the model W China to be representative of the structure in the upper mantle transition zone beneath western China. The model shows a rapid increase in velocity between 550 to 600 km and low velocity gradients from 600 to 690 km.

References

Aki, K. and P. G. Richards (1980). *Quantitative Seismology: Theory and Methods*, W.H. Freeman and Co., Vol. 1 & 2.

Bullen, K.E. (1963). *An Introduction to the Theory of Seismology*, 3rd ed., Cambridge Univ. Press. 381pp.

Capon, J., R.J. Greenfield, and R.J. Kolker (1967). Multidimensional maximum-likelihood processing of large aperture seismic array, *Proc. IEEE*, **55**, 192-211.

Chapman, C.H. (1978). A new method for computing synthetic seismograms, *Geophys. J. R. astr. Soc.*, **54**, 481-518.

Filson, J. (1975). Array seismology, *Annal. Earth Sciences*, 157-181.

Johnson, Don H. and Dan E. Dudgeon (1993). *Array Signal Processing: Concepts and technique*, Prentice-Hall, Inc., Englewood Cliffs, New Jersey, 533pp.

Kennett, B.L.N. and E.R. Engdahl (1991). Traveltimes for global earthquake location and phase identification, *Geophys. J. Int.*, 105, 429-465.

Kim, W. Y., V. V. Kazakov, A. G. Vanchugov and D. W. Simpson (1996). Broadband and array observations at low noise sites in Kazakstan: Opportunity for seismic monitoring of Comprehensive Test Ban Treaty, pp 462–482 in *Monitoring a Comprehensive Test Ban Treaty*, eds. E.S. Husebye and A.M. Dainty, Kluwer, Dordrecht.

King, D. W., R. F. Mereu and K. J. Muirhead (1973). The measurement of apparent velocity and azimuth using adaptive processing techniques on data from the Warramunga seismic array, *Geophys. J.*, **35**, 137–167.

Mykkeltveit, S., F. Ringdal, T. Kvørna and R. W. Alewine (1990). Application of regional arrays in seismic verification research, *Bull. Seism. Soc. Am.*, **80**, 1777 – 1800.

Niazi, M. (1966). Corrections to apparent azimuths and travel-time gradient for a dipping Mohorovicic discontinuity, *Bull. Seism. Soc. Am.*, **56**, 491–509.

Simpson, D. W., R. F. Mereu and D. W. King (1974). An array study of P-wave velocities in the upper mantle transition zone beneath northeastern Australia, *Bull. Seism. Soc. Am.*, **64**, 1757–1788.

Slichter, L. B. (1932). The theory of the interpretation of seismic travel time curves in horizontal structures, *Physics*, **3**, 273–295.

Zengni, T. G. (1970). A note on an azimuthal correction for dT/dΔ for a single dipping plane interface, *Bull. Seism. Soc. Am.*, **60**, 299–306.

Table 1. Events used in this study*.

N	Date dd/mm/yr	Origin Time hh:mm:sec	Lat. (°)	Long. (°)	depth (km)	m_b	Dist (°)	Az (°)
1	02/12/95	10:56:58.8	33.280	93.386	27	4.8	20.48	332.3
2	03/05/95	07:00:00.4	24.670	99.965	33	4.4	30.76	333.1
3	03/18/95	18:02:36.6	42.422	87.199	22	5.2	10.12	327.1
4	04/14/95	19:53:34.5	29.613	115.616	10	4.0	34.72	317.8
5	04/24/95	16:13:11.4	22.736	102.906	33	4.7	33.72	331.9
6	04/26/95	03:46:32.8	28.895	103.778	33	4.9	28.85	325.9
7	04/26/95	20:11:20.8	32.700	102.388	33	4.1	25.06	322.7
8	04/26/95	22:46:27.0	37.248	105.718	33	4.2	23.50	313.4
9	05/02/95	11:48:11.6	43.776	84.660	33	5.5	08.01	330.9
10	05/08/95	18:37:33.7	33.329	103.592	33	4.7	25.19	320.9
11	05/12/95	03:43:49.0	23.688	100.415	33	4.8	31.82	333.4
12	05/19/95	11:45:37.3	41.720	92.894	11	4.2	13.31	316.9
13	05/23/95	17:17:29.0	32.455	93.560	33	4.8	21.28	333.0
14	05/30/95	23:43:51.8	27.141	95.659	33	4.9	26.86	335.6
15	06/03/95	11:29:25.2	28.080	102.897	33	4.3	29.10	327.4
16	06/10/95	05:08:55.7	31.685	104.208	33	4.7	26.80	322.4
17	06/11/95	23:39:51.1	31.887	92.446	33	4.2	21.38	335.3
18	06/12/95	03:37:30.0	31.781	104.256	10	4.4	26.75	322.3
19	06/12/95	14:47:58.3	39.218	95.292	24	5.1	16.39	319.6
20	06/21/95	08:28:41.8	37.729	106.422	33	4.5	23.58	312.1
21	06/27/95	05:48:25.1	26.209	96.342	33	4.6	27.96	335.6
22	06/29/95	23:03:46.2	21.925	98.943	33	4.9	32.84	335.9
23	07/04/95	18:29:45.4	30.386	94.797	33	4.0	23.60	333.6
24	07/05/95	23:38:48.9	42.513	86.678	33	4.5	09.84	328.3
25	07/09/95	15:56:28.2	35.976	100.073	33	5.2	21.31	320.1
26	07/09/95	20:31:31.4	21.984	99.159	10	5.7	32.87	335.7
27	07/09/95	20:33:32.5	21.725	99.086	10	5.0	33.07	335.9
28	07/09/95	21:29:14.7	21.885	99.116	10	4.9	32.94	335.8
29	07/10/95	22:43:16.0	21.984	99.119	10	4.7	32.85	335.7
30	07/11/95	21:46:39.7	21.966	99.196	13	6.1	32.90	335.6
31	07/11/95	22:20:33.4	22.690	100.099	10	4.2	32.59	334.3
32	07/11/95	22:37:07.1	21.808	98.945	10	4.5	32.95	336.0
33	07/11/95	23:16:16.8	21.467	98.548	10	4.4	33.11	336.6
34	07/12/95	03:57:00.4	21.123	99.034	10	4.2	33.60	336.3
35	07/12/95	06:02:56.1	21.886	99.157	10	4.3	32.95	335.7
36	07/12/95	08:14:33.8	22.041	99.309	10	4.2	32.87	335.5
37	07/12/95	09:44:53.1	21.841	99.161	10	4.3	33.00	335.8
38	07/14/95	07:29:36.9	21.806	99.115	10	4.6	33.01	335.8
39	07/16/95	09:27:12.5	30.317	94.828	33	4.9	23.67	333.7
40	07/18/95	11:14:07.2	21.844	99.038	10	4.0	32.95	335.9
41	07/18/95	21:33:41.7	22.005	99.138	10	4.8	32.84	335.7
42	07/19/95	16:08:22.6	30.321	94.866	33	4.9	23.68	333.6
43	07/21/95	22:44:04.5	36.427	103.123	13	5.7	22.61	316.6
44	07/22/95	00:06:06.3	36.414	103.244	10	4.2	22.68	316.5
45	07/23/95	05:39:49.5	22.015	98.907	10	4.4	32.74	335.9

Table 1 Continued

46	07/25/95	15:41:24.5	23.196	105.845	10	4.2	34.66	329.2
47	07/30/95	13:03:59.9	32.142	101.440	33	4.4	25.03	324.3
48	07/30/95	19:43:09.2	21.987	99.052	33	4.1	32.82	335.8
49	08/02/95	01:46:31.6	26.741	103.053	33	4.4	30.31	328.6
50	08/02/95	11:59:43.9	41.631	88.447	10	4.1	11.30	326.1
51	08/07/95	03:27:16.6	21.931	99.218	33	4.1	32.94	335.7
52	08/17/95	00:59:57.7	41.559	88.800	0	6.0	11.50	325.4
53	08/22/95	00:46:53.3	30.257	97.203	33	4.2	24.68	330.9
54	08/28/95	11:46:05.6	38.186	89.001	33	4.9	14.48	332.5
55	08/30/95	12:52:59.6	44.098	84.117	33	4.5	07.54	331.9
56	09/02/95	18:25:26.5	37.956	91.395	33	4.5	15.61	328.3
57	09/04/95	08:55:35.6	26.535	101.638	18	4.2	29.84	330.0
58	09/04/95	18:43:45.1	43.903	87.436	33	4.1	09.02	321.2
59	09/05/95	16:19:17.0	27.094	96.680	33	4.3	27.28	334.5
60	09/06/95	00:11:23.1	29.156	104.012	33	4.3	28.75	325.4
61	10/06/95	14:26:04.7	33.407	93.467	33	4.4	20.40	332.0
62	10/09/95	17:48:23.8	25.075	97.727	33	4.4	29.51	334.9
63	10/14/95	04:50:32.5	33.158	92.783	33	4.2	20.36	333.3
64	10/14/95	05:52:46.5	44.422	86.926	33	4.0	08.39	320.6
65	10/21/95	20:10:49.0	36.215	103.301	33	4.4	22.86	316.8
66	10/23/95	22:46:50.8	26.003	102.227	10	5.8	30.57	329.9
67	10/23/95	23:47:10.3	25.791	102.561	33	4.5	30.90	329.8
68	10/24/95	00:09:54.7	25.846	102.146	10	4.2	30.67	330.1
69	10/24/95	00:29:03.5	25.847	102.106	10	4.3	30.65	330.1
70	10/24/95	01:00:44.0	25.858	102.223	10	4.3	30.69	330.0
71	10/24/95	01:19:11.5	25.830	102.236	10	4.3	30.72	330.1
72	10/24/95	01:40:01.7	25.923	102.365	10	4.2	30.70	329.9
73	10/24/95	02:11:59.4	25.801	102.067	10	4.3	30.67	330.2
74	10/24/95	08:08:14.4	25.886	102.547	10	4.6	30.81	329.7
75	10/24/95	10:45:07.9	25.719	102.281	33	4.2	30.84	330.1
76	10/24/95	17:29:55.9	25.754	102.098	10	4.4	30.73	330.2
77	10/24/95	17:43:26.1	25.914	102.340	10	4.7	30.70	329.9
78	10/24/95	22:32:54.6	25.906	102.163	10	4.7	30.62	330.1
79	10/24/95	23:13:15.8	25.777	102.110	10	4.4	30.71	330.2
80	10/25/95	02:42:57.0	25.903	102.430	10	4.3	30.75	329.8
81	10/25/95	03:16:32.3	25.963	102.210	10	4.4	30.59	330.0
82	10/25/95	04:21:52.1	25.773	102.256	10	4.4	30.78	330.1
83	10/25/95	17:33:39.0	25.879	102.189	10	4.1	30.66	330.1
84	10/26/95	13:19:34.9	25.738	102.045	10	4.0	30.72	330.3
85	10/27/95	02:05:36.4	25.896	102.201	10	4.3	30.65	330.0
86	10/27/95	08:52:34.6	36.696	92.080	33	4.9	16.97	329.4
87	10/28/95	12:55:05.2	26.020	102.300	10	4.4	30.59	329.8
88	10/28/95	20:36:03.7	25.958	102.257	10	4.5	30.62	329.9
89	10/29/95	15:46:01.5	25.667	102.083	33	4.2	30.80	330.3
90	10/29/95	17:18:42.3	25.852	102.219	10	4.5	30.70	330.1
91	11/01/95	08:10:07.8	25.868	102.339	10	4.8	30.74	329.9
92	11/01/95	15:29:36.2	25.926	102.247	11	4.5	30.64	330.0
93	11/02/95	21:26:51.2	25.836	102.069	10	4.0	30.64	330.2
94	11/04/95	20:07:39.8	33.018	92.140	33	4.0	20.24	334.4
95	11/05/95	17:14:53.6	32.896	92.201	24	5.1	20.38	334.5
96	11/07/95	03:50:09.4	26.004	102.471	10	4.3	30.68	329.7
97	11/07/95	20:47:07.2	25.872	102.425	20	4.6	30.77	329.9

Table 1 Continued

98	11/09/95	20:55:17.6	22.058	102.724	33	4.4	34.24	332.5
99	11/11/95	14:29:27.0	34.935	104.080	10	4.3	24.23	318.2
100	11/18/95	04:48:11.7	25.673	102.342	20	4.0	30.91	330.1
101	11/29/95	14:23:08.7	25.425	102.142	10	4.0	31.03	330.5
102	12/03/95	16:17:23.8	25.984	102.193	20	4.1	30.57	330.0
103	12/07/95	01:28:50.1	36.406	100.114	33	4.0	21.00	319.4
104	12/12/95	05:42:32.2	26.852	96.059	33	5.1	27.27	335.4
105	12/12/95	17:31:16.8	42.117	86.911	33	4.3	10.27	328.8
106	12/18/95	04:57:04.7	34.511	97.351	33	5.3	21.13	325.4
107	12/20/95	10:07:58.7	34.488	97.474	33	5.0	21.20	325.3
108	12/26/95	03:31:09.7	29.313	105.453	33	4.2	29.35	324.1
109	01/02/96	11:37:41.1	38.515	102.845	33	4.2	20.98	313.1
110	01/04/96	02:55:45.5	38.140	102.815	33	4.1	21.22	313.9
111	01/04/96	03:49:27.6	38.740	104.598	33	4.7	21.84	311.5
112	01/04/96	07:26:52.4	36.218	100.491	33	4.2	21.34	319.3
113	01/09/96	06:27:54.4	43.703	85.654	33	5.2	08.44	327.6
114	01/16/96	00:08:18.5	29.458	105.605	33	4.2	29.31	323.9
115	01/18/96	00:19:54.5	23.894	94.597	33	4.0	29.48	339.1
116	01/26/96	02:21:11.2	30.873	91.478	33	5.1	21.98	337.7
117	02/02/96	22:59:55.5	22.141	103.164	10	4.2	34.36	332.1
118	02/03/96	11:14:19.8	27.299	100.341	10	6.3	28.61	330.5
119	02/03/96	11:24:01.9	27.280	100.820	10	4.5	28.83	330.1
120	02/03/96	11:39:41.9	27.267	100.318	10	4.9	28.62	330.6
121	02/03/96	11:58:24.5	27.151	100.331	10	4.6	28.73	330.6
122	02/03/96	12:03:28.8	27.431	100.877	10	4.2	28.73	329.9
123	02/03/96	12:08:16.6	27.207	100.358	10	5.0	28.69	330.6
124	02/03/96	12:14:52.1	27.053	100.465	10	4.6	28.88	330.6
125	02/03/96	12:36:59.6	27.165	100.539	10	4.0	28.81	330.4
126	02/03/96	12:49:11.1	27.115	100.584	10	4.0	28.87	330.4
127	02/03/96	13:17:30.0	27.214	100.254	10	4.3	28.64	330.7
128	02/03/96	13:35:06.4	27.150	100.365	10	4.0	28.75	330.6
129	02/03/96	14:00:14.7	27.316	100.654	10	4.2	28.73	330.2
130	02/03/96	14:19:36.6	27.131	100.379	10	4.4	28.77	330.6
131	02/03/96	14:56:27.2	27.372	100.380	10	4.1	28.56	330.4
132	02/03/96	15:10:02.5	26.798	100.124	10	4.0	28.95	331.2
133	02/03/96	17:49:39.1	27.310	100.724	10	4.0	28.77	330.1
134	02/03/96	19:38:58.1	27.079	100.527	10	4.7	28.88	330.5
135	02/04/96	04:37:47.9	26.976	100.447	10	4.1	28.93	330.7
136	02/04/96	16:58:05.8	27.050	100.383	10	5.5	28.84	330.7
137	02/04/96	22:57:48.4	26.972	100.343	10	4.6	28.89	330.8
138	02/05/96	03:26:10.5	27.010	100.424	10	4.7	28.89	330.7
139	02/05/96	14:36:06.4	21.366	97.724	33	4.1	32.90	337.4
140	02/05/96	19:40:21.6	26.898	100.305	10	4.3	28.94	330.9
141	02/06/96	01:42:32.5	27.049	100.314	10	4.3	28.81	330.8
142	02/06/96	07:36:13.8	27.247	100.418	10	5.3	28.68	330.5
143	02/06/96	20:08:57.4	27.241	100.530	10	5.2	28.74	330.4
144	02/07/96	07:19:41.4	26.969	100.505	10	4.8	28.96	330.6
145	02/07/96	15:29:23.9	27.125	100.894	10	4.2	29.00	330.1
146	02/07/96	21:04:27.4	27.247	100.691	10	4.3	28.80	330.2
147	02/08/96	15:54:07.9	25.408	96.991	33	4.2	28.93	335.5
148	02/08/96	22:46:40.2	27.019	100.499	10	4.4	28.92	330.6

Table 1 Continued

149	02/11/96	08:43:28.2	27.529	101.301	10	4.4	28.83	329.4
150	02/15/96	01:09:50.7	27.252	100.606	33	4.3	28.76	330.3
151	02/16/96	03:02:22.5	28.863	92.900	11	4.4	24.30	337.5
152	02/24/96	00:57:39.0	27.208	100.278	33	4.3	28.66	330.6
153	02/28/96	11:22:02.0	29.099	104.737	33	5.1	29.16	324.9
154	02/28/96	23:21:48.4	27.045	100.279	33	4.1	28.80	330.8
155	03/13/96	03:52:14.3	27.039	100.389	33	4.7	28.85	330.7
156	03/16/96	06:46:53.5	27.139	100.625	33	4.1	28.87	330.4
157	03/19/96	10:48:38.8	24.946	96.418	33	4.4	29.14	336.4
158	03/20/96	02:11:21.9	42.182	87.627	25	4.8	10.50	326.6
159	03/21/96	22:34:04.8	26.351	98.450	10	4.3	28.65	333.2
160	03/31/96	03:07:14.0	43.019	88.680	33	4.2	10.28	321.2
161	04/09/96	22:00:46.1	20.282	98.719	33	4.0	34.26	337.1
162	04/10/96	04:13:18.4	24.026	96.714	33	4.1	30.09	336.7
163	04/16/96	21:24:22.6	26.659	100.152	10	4.2	29.08	331.2
164	04/22/96	04:43:21.6	30.048	92.074	33	4.5	22.93	337.6
165	04/22/96	20:24:40.1	44.141	86.925	33	4.0	08.61	321.8

Table 2. W China *P* velocity model*.

Depth (km)	V_P (km/s)	Depth (km)	V_P (km/s)	Depth (km)	V_P (km/s)
0	5.80	260	8.54	530	9.65
10	5.80	270	8.57	540	9.70
20	5.80	280	8.61	550	9.76
20	6.50	290	8.64	560	9.84
30	6.50	300	8.68	570	9.96
35	6.50	310	8.71	580	10.10
35	8.00	320	8.75	590	10.21
40	8.04	330	8.78	600	10.32
50	8.04	340	8.82	610	10.34
60	8.04	350	8.85	620	10.36
70	8.04	360	8.89	630	10.37
80	8.04	370	8.92	640	10.38
90	8.04	380	8.96	650	10.40
100	8.04	390	8.99	660	10.40
110	8.05	400	9.03	670	10.42
120	8.06	410	9.07	680	10.45
130	8.09	417	9.13	689	10.55
140	8.12	417	9.30	689	10.90
150	8.16	420	9.31	690	10.92
160	8.19	430	9.34	700	10.96
170	8.22	440	9.37	710	10.99
180	8.26	450	9.41	720	11.03
190	8.29	460	9.45	730	11.06
200	8.33	470	9.49	740	11.10
210	8.36	480	9.52	750	11.14
220	8.40	490	9.56	760	11.16
230	8.43	500	9.58	770	11.17
240	8.47	510	9.60	780	11.18
250	8.50	520	9.62	790	11.19

* The crust and upper most mantle model is IASPEI 91 model.

Figure Captions

Fig. 1. Location of the cross-array in Kurchatov, Kazakstan. The configuration of the 21-element array with a station spacing of 2.25 km is depicted. Other seismographic stations in central Asia are also shown for reference.

Fig. 2. Epicenters of the earthquakes used in this study are plotted on a map of topographic relief. The size of the circle represents the size of the earthquake, and the focal mechanisms (Harvard CMT solutions) of the earthquakes in the region are plotted as beach balls. P-wave signals from most of the earthquakes selected for analysis propagate through the crust and upper mantle beneath the Tibetan Plateau andthe Northern Tien-Shan mountains in western China.

Fig. 3. Seismic record section showing the waveforms from earthquakes in the distance range 10° to 20°. Records at the center of the array (C21) are plotted with a reduction velocity of 10 km/s (=11.12 s/deg) and predicted travel time curves for focal depth = 15 km for various P-wave branches are indicated. The A–B branch is for Pn arrivals, the C–D branch for first arriving P waves whose rays have turning point below the 410 km discontinuity, and G–H is a portion of the P travel time branch corresponding to rays turning below the "660 km discontinuity" (later in this paper, estimated as having a depth of about 680 km). Note that record from each event is plotted here without adjusting for its focal depth.

Fig. 4. A synthetic record section showing the first as well as later arrival P waves in the IASPEI 91 model for a focal depth of 15 km. The source mechanism from an event on 12/18/95 (04:57, M=5.7) is used to calculate amplitude and travel times using the WKBJ seismogram method.

Fig. 5. An example of the method of determination of slowness and azimuth by using a weighted, delay-and-sum beamform. The event analyzed occurred on 05/23/95 (17:17, $\Delta = 21.28°$, $m_b =$ 4.8, h =33 km, PDE). (a) the top trace is the reference station waveform and the bottom trace is the array beam calculated using the slowness and azimuth determined from the time window indicated; (b) azimuth (cross), slowness (circle) and beam power (triangle) determined at each time window are plotted vs time; (c) contour of the beam power for the best beam determination; (d) waveforms at all stations are plotted, each with its appropriate delay, and the top trace is the array beam.

Fig. 6. (a) Combined first arrival travel time and slowness data reduced to a surface focus are plotted with a reduction slowness of 11.12 s/deg (thick lines), and showing corresponding slownesses also corrected for the local structure (thin lines). Slope lines plotted using the slope of the measured slowness. (b) The slownesses of the first arrivals corrected to surface focus are plotted vs. distance (open circles), and showing corresponding slownesses corrected also for the local structure (solid circles).

Fig. 7. Slownesses corrected for local structure and reduced to the surface focus are plotted against epicentral distance. The slownesses are fitted by several polynomial curves and travel time branches are marked by letters.

Fig. 8. (a) Slownesses corrected for local structure and reduced to the surface focus are plotted against epicentral distance. The slownesses are fitted by several polynomial curves identified by corresponding P-wave travel time branches, (b) W China upper mantle model (*solid line*) obtained in this study is compared with the IASPEI 91 model (*dashed line*).

Fig. 9. Selected waveform data are plotted with reduced velocity of 11.12 s/deg and travel time curves predicted by the W China model are superimposed for comparison.

Kurchatov Cross-Arrays in Kazakstan
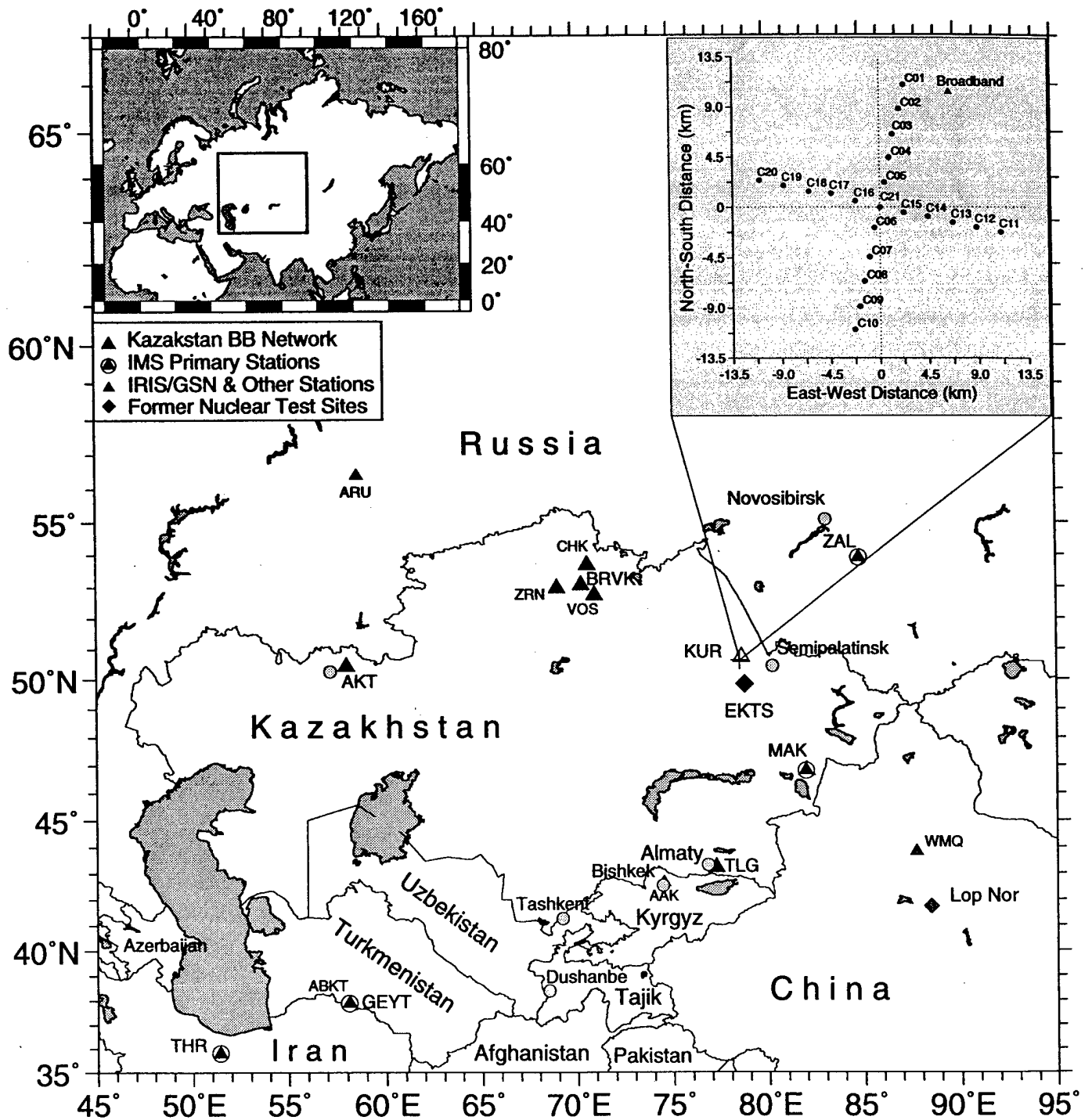
Fig. 1

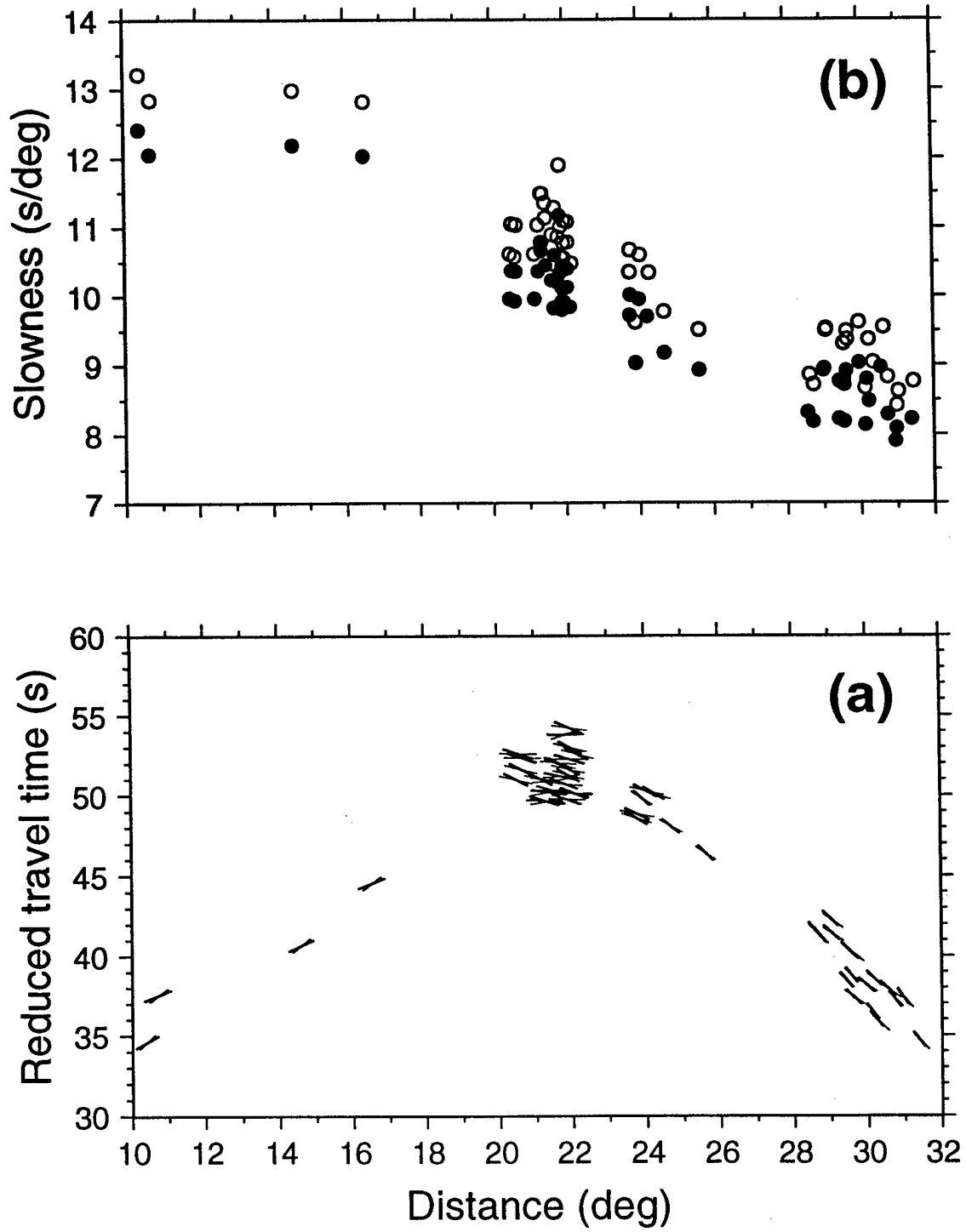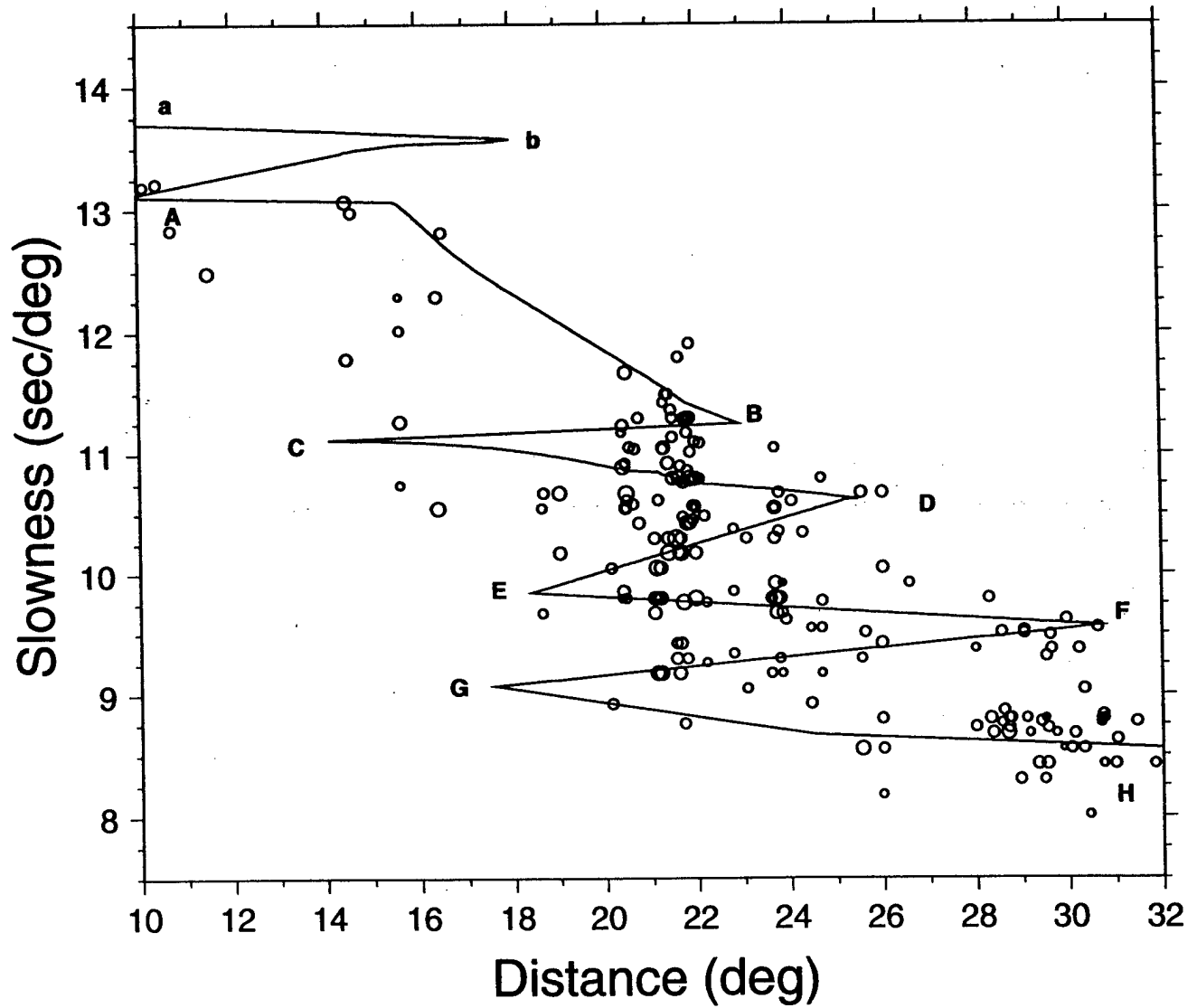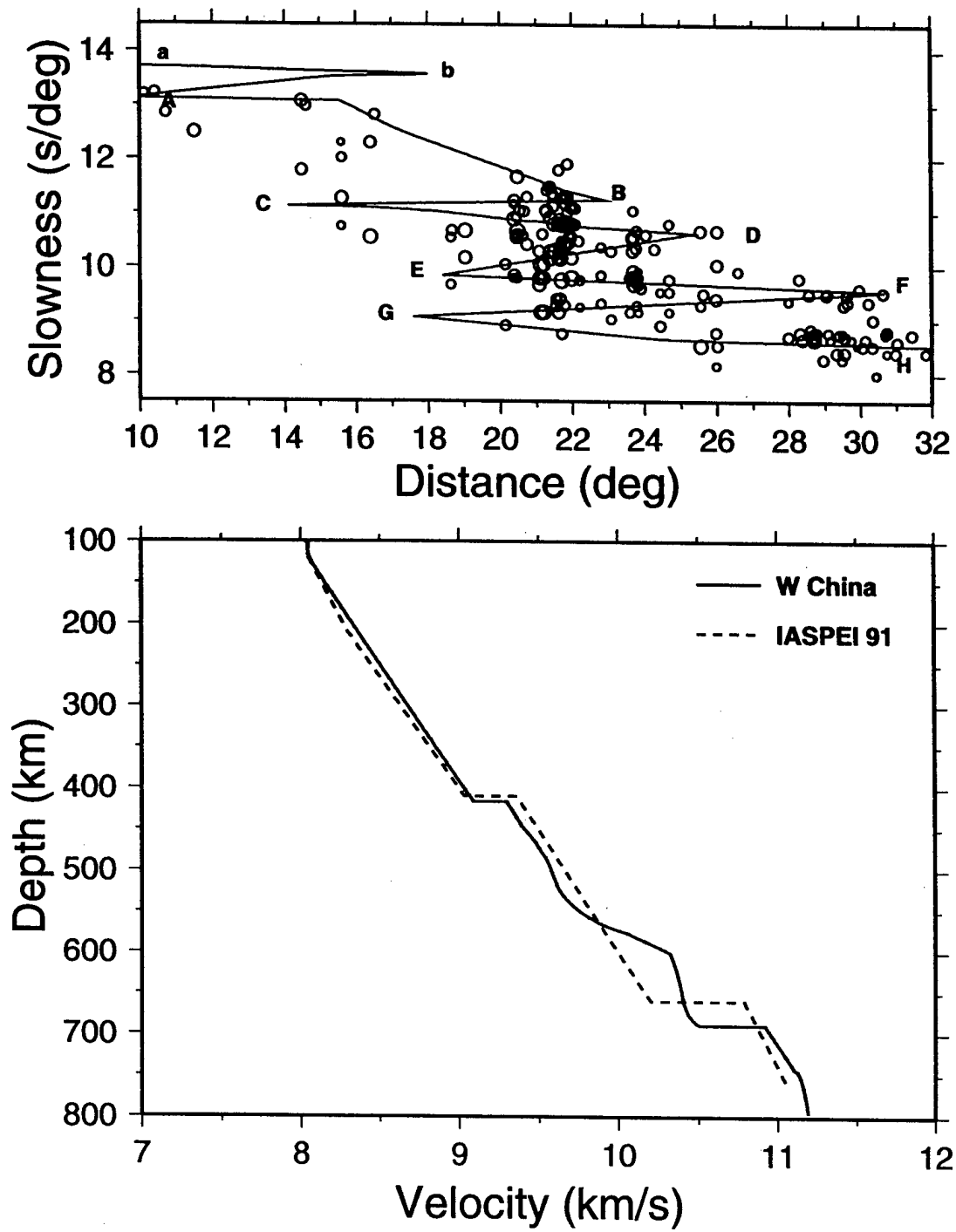# Events in Tibet Plateau & Western China
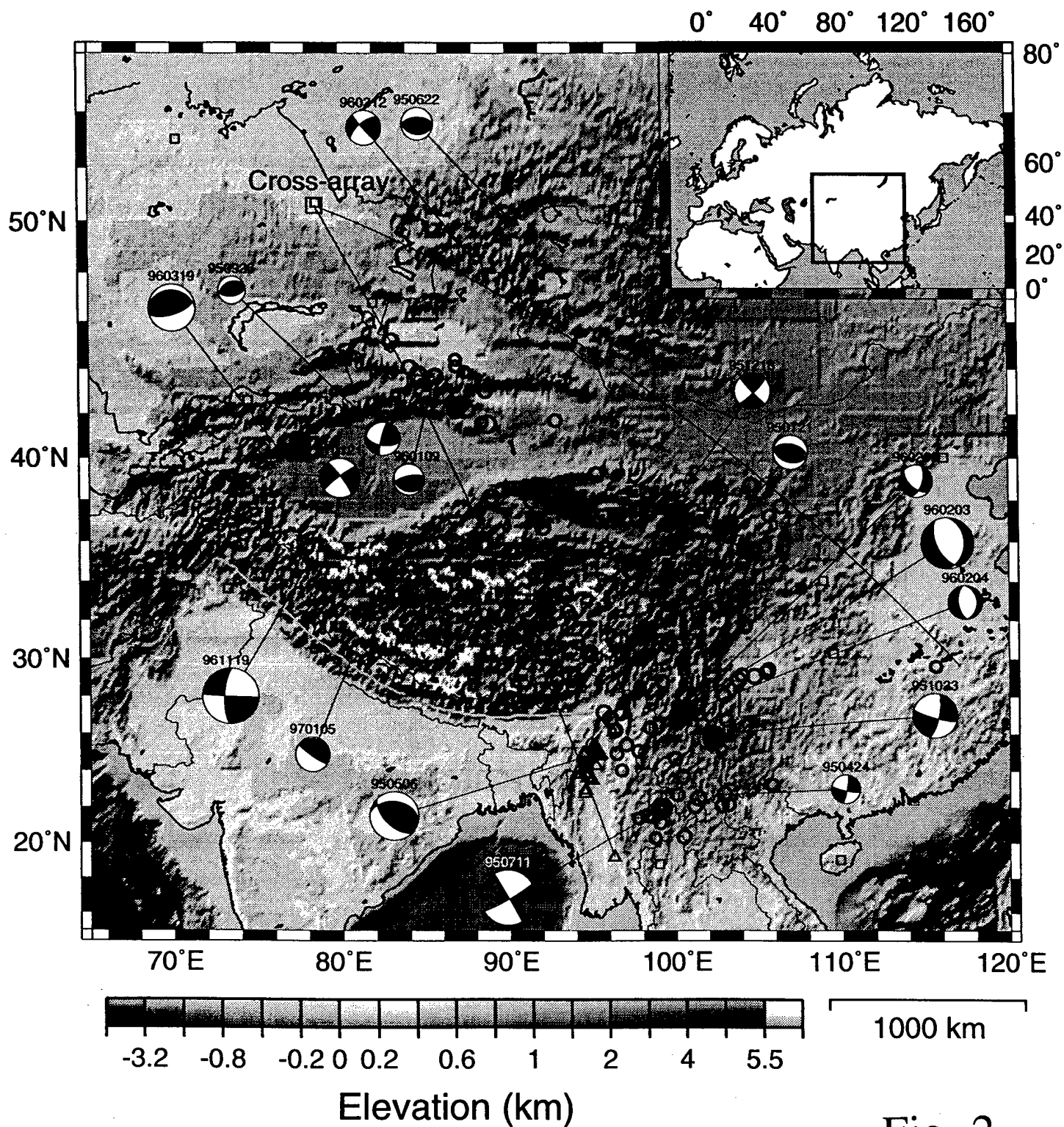
Fig. 2
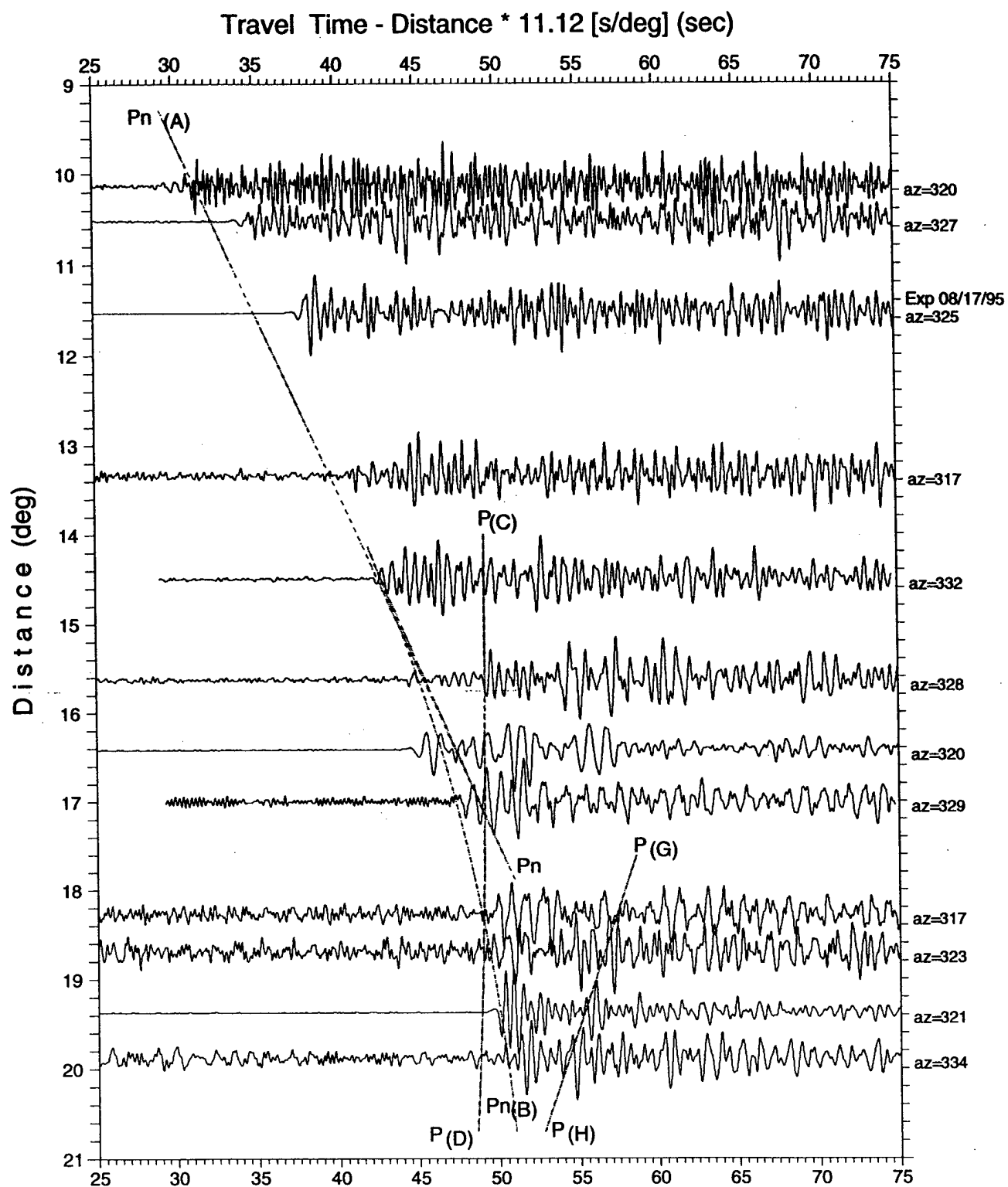
Fig. 3
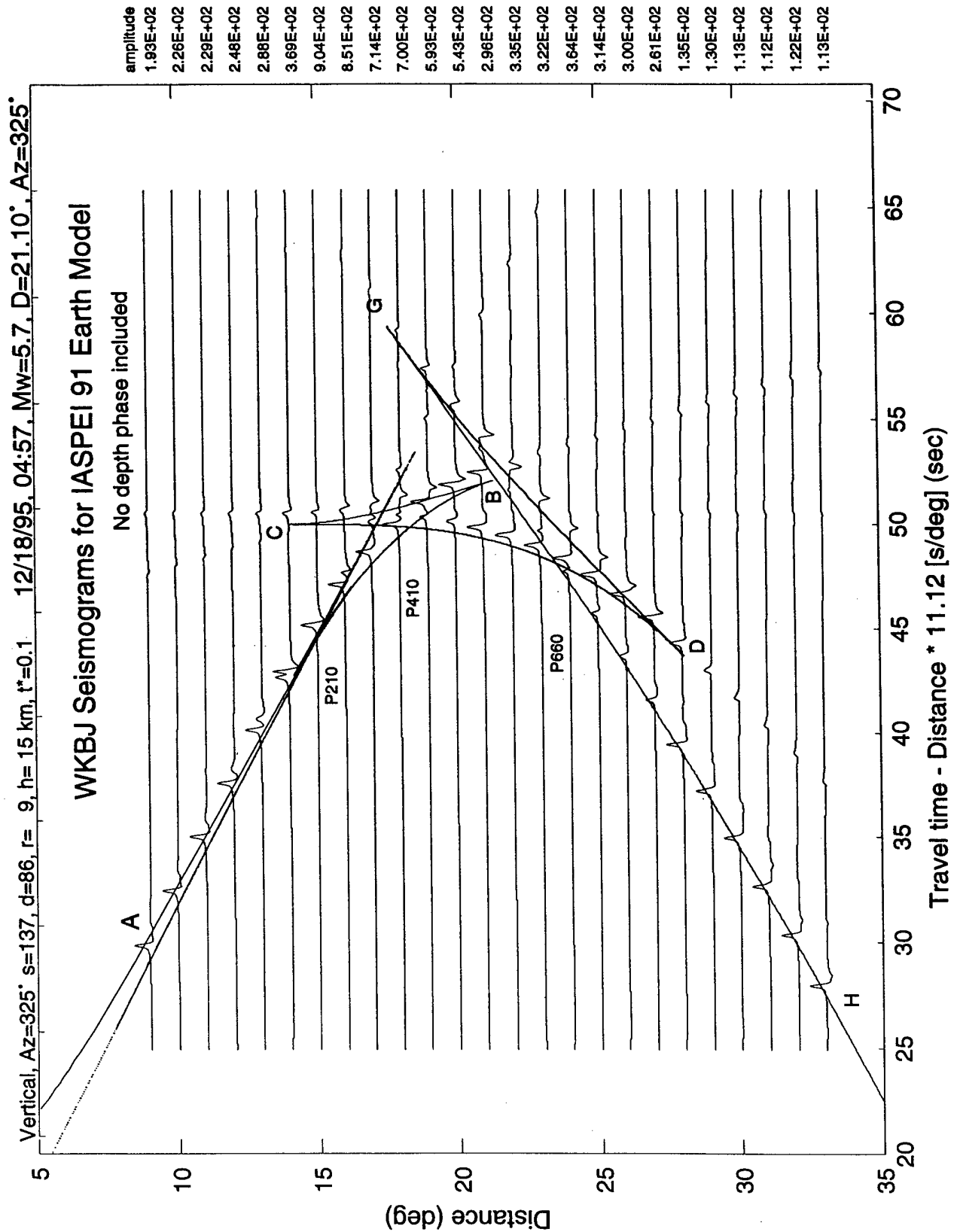
Fig. 4
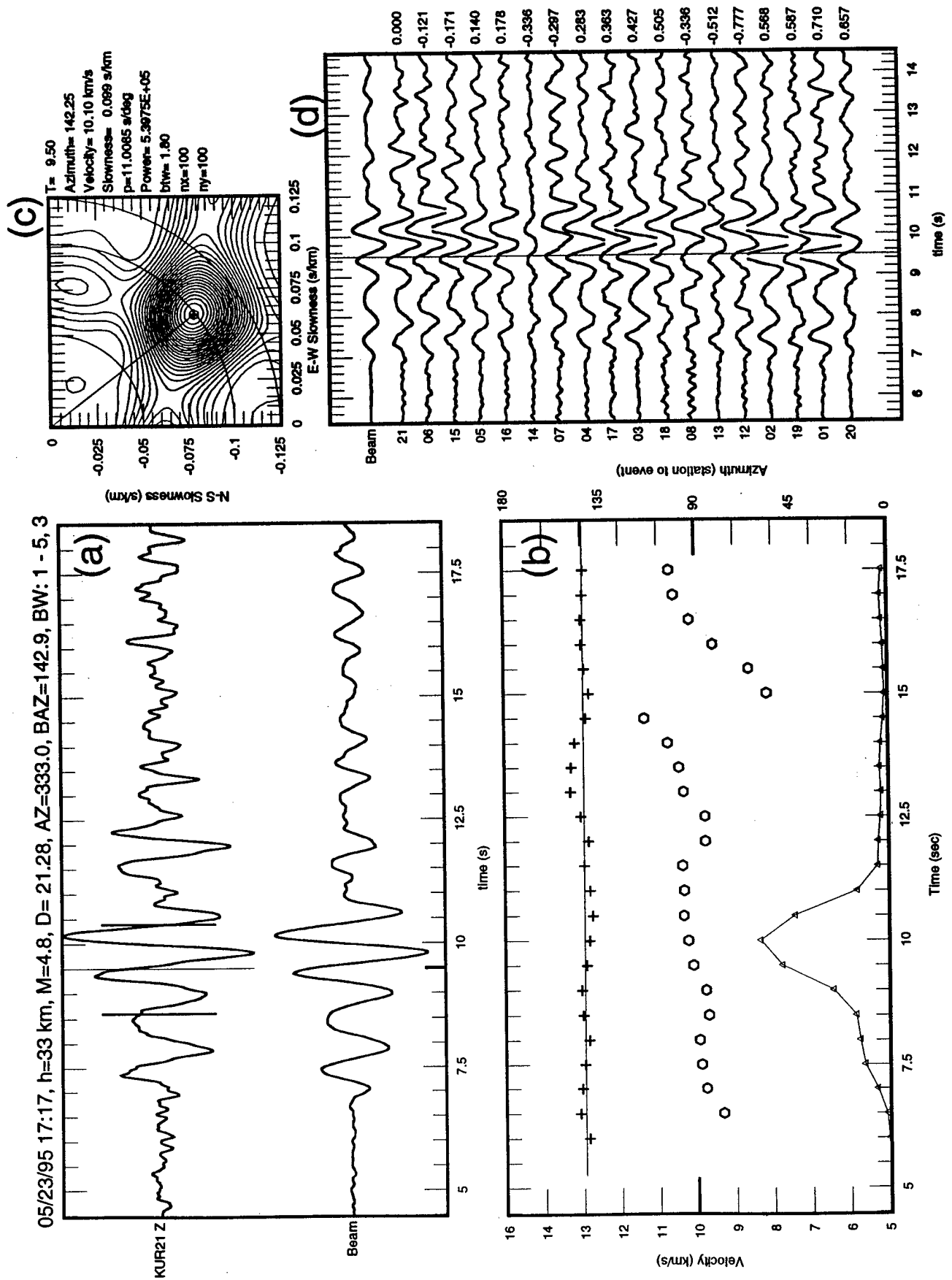
Fig. 5

Fig. 6

Slownesses

Fig. 7

Fig. 8

Waveform Data

Fig. 9